

RESEARCH ARTICLE | Neural Circuits

High-density extracellular probes reveal dendritic backpropagation and facilitate neuron classification

 **Xiaoxuan Jia, Joshua H. Siegle, Corbett Bennett, Samuel D. Gale, Daniel J. Denman, Christof Koch, and Shawn R. Olsen**

Allen Institute for Brain Science, Seattle, Washington

Submitted 9 October 2018; accepted in final form 25 February 2019

Jia X, Siegle JH, Bennett C, Gale SD, Denman DJ, Koch C, Olsen SR. High-density extracellular probes reveal dendritic backpropagation and facilitate neuron classification. *J Neurophysiol* 121: 1831–1847, 2019. First published March 6, 2019; doi:10.1152/jn.00680.2018.—Different neuron types serve distinct roles in neural processing. Extracellular electrical recordings are extensively used to study brain function but are typically blind to cell identity. Morphoelectrical properties of neurons measured on spatially dense electrode arrays have the potential to distinguish neuron types. We used high-density silicon probes to record from cortical and subcortical regions of the mouse brain. Extracellular waveforms of each neuron were detected across many channels and showed distinct spatiotemporal profiles among brain regions. Classification of neurons by brain region was improved with multichannel compared with single-channel waveforms. In visual cortex, unsupervised clustering identified the canonical regular-spiking (RS) and fast-spiking (FS) classes but also indicated a subclass of RS units with unidirectional backpropagating action potentials (BAPs). Moreover, BAPs were observed in many hippocampal RS cells. Overall, waveform analysis of spikes from high-density probes aids neuron identification and can reveal dendritic backpropagation.

NEW & NOTEWORTHY It is challenging to identify neuron types with extracellular electrophysiology *in vivo*. We show that spatiotemporal action potentials measured on high-density electrode arrays can capture cell type-specific morphoelectrical properties, allowing classification of neurons across brain structures and within the cortex. Moreover, backpropagating action potentials are reliably detected *in vivo* from subpopulations of cortical and hippocampal neurons. Together, these results enhance the utility of dense extracellular electrophysiology for cell-type interrogation of brain network function.

backpropagating action potentials; BAPs; classification; extracellular waveform; *in vivo*; Neuropixels

INTRODUCTION

Brain networks are composed of diverse cell types with distinct roles in neural dynamics and processing. For example, in the neocortex, excitatory pyramidal neurons provide local recurrent processing and send long-range projections for information propagation (Harris and Shepherd 2015; Spruston 2008), whereas inhibitory neurons perform gain modulation, control spike timing and rhythms, and shape receptive field

properties (Isaacson and Scanziani 2011; Kepecs and Fishell 2014; Markram et al. 2004). Thus a mechanistic understanding of brain function requires a cell type-specific approach. Neuronal cell types are defined by various properties including gene expression, morphology, physiology, and connectivity (Baden et al. 2016; Gouwens et al. 2018; Harris and Shepherd 2015; Kim et al. 2017; Markram et al. 2004; Tasic et al. 2016; Zeng and Sanes 2017). Although imaging of genetically encoded calcium sensors can be used to measure activity of identified neuronal subpopulations (Luo et al. 2008), this method has much lower temporal resolution compared with electrophysiological recordings and can be difficult in deep brain structures. Antidromic stimulation has historically been a powerful method for identifying cell types on the basis of long-range projection targets (Li et al. 2015; Lipski 1981; Sommer and Wurtz 2004) but typically is not sufficient for identifying local cell types. Optotagging can link extracellular spike measurements to cell types by directly photo-stimulating cells that express a light-sensitive opsin under genetic control (Cohen et al. 2012; Kvitsiani et al. 2013; Lima et al. 2009), but this is largely restricted to transgenic systems and usually only labels one cell population per experiment.

Extracellular electrical recordings are widely used to measure single-neuron spiking activity *in vivo* during active behavior. Previous studies have shown that action potential shape can provide information about the cell type being recorded (Kawaguchi 1993; McCormick et al. 1985). Conventionally, single-unit waveforms are divided into two broad categories: regular spiking (RS), which represent pyramidal neurons and some inhibitory neurons, and fast spiking (FS), which largely correspond to inhibitory interneurons (Andermann et al. 2004; Bortone et al. 2014; Bruno and Simons 2002; Mitchell et al. 2007; Niell and Stryker 2008; Peyrache et al. 2012; Sirota et al. 2008; Swadlow 2003). In general, RS neurons are characterized by broader action potentials with spike frequency adaptation, whereas FS neurons have relatively brief-duration action potentials with little adaptation (Hu et al. 2014; Markram et al. 2004). This classification is supported by the correlation between extracellular waveform and intrinsic electrophysiological properties (Anastassiou et al. 2015; Buzsáki et al. 2012; Gold et al. 2006; Henze et al. 2000). The ability to more generally link cell classes to extracellular action potential waveform features would enhance many studies of circuit-level functions in the brain.

Address for reprint requests and other correspondence: X. Jia, Allen Institute for Brain Science, 615 Westlake Ave. N, Seattle, WA 98109 (e-mail: jxiao@alleninstitute.org).

Recent developments in high-density silicon probe technology permit enhanced spatial sampling of extracellular waveforms from single units *in vivo* (Blanche et al. 2005; Chung et al. 2018; Jun et al. 2017; Neto et al. 2016; Rutherford and Paul 2015; Scholvin et al. 2016; Shobe et al. 2015). The close spacing of electrode contacts on these probes (25 μm or less) allows each unit's waveform to be detected by many sites simultaneously, thereby providing a rich spatiotemporal extracellular waveform profile. Since both electrical and morphological properties are key attributes of cell types (Ascoli et al. 2007; Gouwens et al. 2018; Jiang et al. 2015; Zeng and Sanes 2017), the densely sampled extracellular waveforms might provide a signature for different cell classes. Indeed, both modeling and empirical studies *in vitro* suggest that such detailed extracellular action potential waveforms can, in principle, be used for cell classification (Buccino et al. 2018; Delgado Ruz and Schultz 2014). Evidence from *in vivo* studies also suggest cell type-specific morphoelectrical properties. For example, backpropagating action potentials (BAPs) (Beresh-

polova et al. 2007; Buzsáki and Kandel 1998; Stuart et al. 1997; Stuart and Sakmann 1994; Waters et al. 2005) are observed in putative pyramidal neurons as traveling waves along linear recording probes, but not in FS neurons (Bereshpolova et al., 2007; Buzsáki and Kandel, 1998). In the current study, we used a new high-density silicon probe, Neuropixels (Jun et al. 2017), to make large-scale electrophysiological recordings in the awake mouse brain and investigated the properties of spatiotemporal extracellular waveform profiles of individual neurons. Specifically, we sought to address whether detailed features from these higher resolution waveforms can facilitate cell classification across different brain regions and within cortex (Fig. 1, A and B).

Diverse morphoelectrical properties across cortical and subcortical structures are well documented in previous studies (Ascoli et al. 2007; Bean 2007; Stuart et al. 1997). For example, most thalamic neurons have symmetric, radial dendrites (Clascá et al. 2012; Jones 2012), whereas cerebellar Purkinje cells have elaborate, highly branched dendritic arbors,

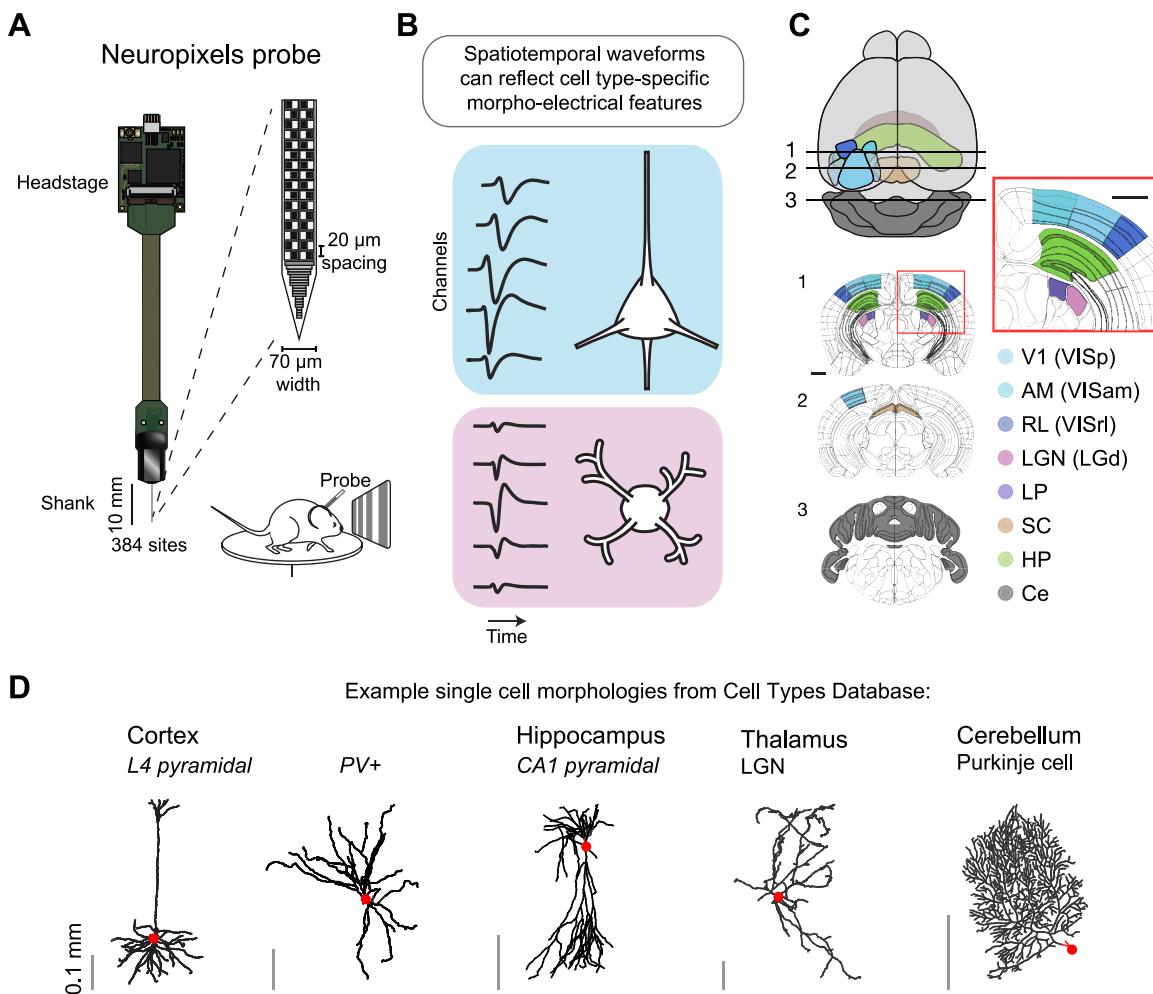


Fig. 1. Experimental setup including regions and example neuron classes. **A:** data are collected with Neuropixels probes inserted into the awake mouse brain. The 384 electrode sites are densely arranged along the linear shank of the silicon probe (20- μm vertical spacing, 2 sites per row). Black squares indicate the location of recording sites. **B:** schematic illustrating our working model showing that extracellular waveforms at different spatial locations relative to the neuron can reflect cell type-specific morphoelectrical features. **C:** illustrations of brain regions targeted for recordings (from Allen Mouse Brain Atlas). In the visual cortex, we recorded from V1 and two higher visual areas, AM and RL (different blues). In subcortical regions, we recorded from dorsal hippocampus (HP; green), lateral geniculate nucleus (LGN; pink), lateral posterior nucleus (LP; purple), superior colliculus (SC; brown), and cerebellum (Ce; gray). Scale bar indicates 1 mm. **D:** example cell reconstructions from different brain regions to illustrate morphological diversity. Reconstructions are from Allen Cell Types Database (<http://celltypes.brain-map.org/>) and NeuroMorpho Database (<http://www.neuromorpho.org/>; Ascoli et al. 2007). Dendrites are shown in black, and cell body location is denoted with a red circle. PV+, parvalbumin expressing.

both of which are distinct from pyramidal neurons that have elongated apical dendrites that support BAPs. Therefore, in this study, we recorded from multiple brain areas to test whether multichannel waveform analysis could reliably identify cells with known morphoelectrical differences. We applied classification and clustering algorithms to single- and multichannel features of extracellular spike waveforms recorded in the visual cortex, hippocampus, thalamus, superior colliculus, and cerebellum of the awake mouse brain (Fig. 1, *C* and *D*). By combining signals from multiple channels, we could more accurately classify neurons from different brain regions. Within the local circuitry of the neocortex and hippocampus, unsupervised clustering recapitulated the conventional RS and FS division but also suggested additional waveform diversity. We validated the FS cluster by using optogenetics to link recordings to genetically identified parvalbumin-expressing (PV+) neurons. A substantial number of RS units in both visual cortex and hippocampus showed evidence of BAPs, but the FS cluster did not. These putative BAPs are reliably observed *in vivo*, and their signature can help differentiate cells within local circuits of the cortex and hippocampus. We conclude that dense sampling of the extracellular waveform with next-generation extracellular probes provides additional information for cell-type and brain region classification based purely on spike waveform, which can complement additional methodologies for dissecting cell type-specific neural network functions.

METHODS

Data Acquisition and Preprocessing

Animal preparation. All experimental procedures were approved by the Allen Institute for Brain Science Institutional Animal Care and Use Committee. For recordings in visual cortex and hippocampus, a metal headframe with a 10-mm circular opening was attached to the skull with Metabond. In the same procedure, a 5-mm-diameter craniotomy was drilled over left visual cortex and sealed with a circular piece of polydimethylsiloxane (PDMS) silicone, ~0.3 mm thick (Heo et al. 2016). Following a 2-wk recovery period, a visual area map was obtained through intrinsic signal imaging (Juavinett et al. 2017). On the day of the experiment, the mouse was placed under light isoflurane anesthesia for ~40 min to remove the silicone window. A ground wire was secured to the skull, and the exposed brain was covered with a layer of 4% agar in artificial cerebrospinal fluid (ACSF). Following recovery from anesthesia, the mouse was head-fixed on the experimental rig. Three or more Neuropixels probes coated in CM-DiI were independently lowered vertically into visual cortex at a rate of 100 $\mu\text{m}/\text{min}$ using a piezo-driven microstage (New Scale Technologies). When the probes reached their final depths of 1,200–1,500 μm , the tip of each probe extended through visual cortex into hippocampus.

For cerebellar recordings, skin and muscle were resected from above the posterior skull to expose the skull above the cerebellum. Animals were fitted with an aluminum head plate with a 5-mm circular opening above the exposed skull. On the day of recording, the animal was anesthetized and burr holes were made in several locations above the cerebellar cortex. The animal was then head-fixed in the recording apparatus and

allowed to recover from anesthesia. For each insertion ($n = 3$ in one mouse), a Neuropixels probe coated in DiI was lowered through a burr hole to a final depth of 3.4–3.6 mm from the pia at a fixed rate of 100 $\mu\text{m}/\text{min}$. The probe was fixed at a roughly 15° angle relative to the dorsal plane of the skull, resulting in a 6°–19° angle relative to the cerebellum surface for each insertion. Recordings extended through multiple ganglionic layers and into the reticular nuclei (Supplemental Fig. S1; supplemental material for this article is available at https://github.com/jiaxx/waveform_classification). The probe was allowed to rest in place for at least 15 min following insertion before data were recorded.

For lateral posterior nucleus (LP), lateral geniculate nucleus (LGN), and superior colliculus (SC) recordings, a metal headframe was attached to the skull with Metabond. One week after surgery, mice were handled (3–5 days) and habituated to head fixation (~2 wk). On the day of recording, the animal was anesthetized with isoflurane and a small burr hole (~200- μm diameter) was drilled according to stereotactic coordinates (in mm relative to lambda, LP/LGN: 1.5–2.2 anterior, 1.9–1.5 lateral; SC: 0.25 anterior, 0.5 lateral). Mice were given 2 h to recover before being head-fixed in the recording apparatus. A Neuropixels probe was coated in DiI and lowered through the burr hole at a rate of 200 $\mu\text{m}/\text{min}$ to a final depth of 3–3.3 (for LP and LGN) or 1.3–1.6 (SC) mm from the brain surface. The probe was allowed to settle for 30 min before recording began. For most mice, recordings were made on 2 consecutive days.

Data acquisition system. *In vivo* recordings were performed in awake, head-fixed mice allowed to run freely on a rotating disk. During the recordings, the mice either passively viewed visual stimuli or remained in the dark. For recordings in visual cortex and hippocampus (HP), data were collected from 11 mice (25 probe insertions). On average, we recorded 64 ± 6 units in cortex per probe insertion. For recordings in LP, LGN, and SC, data were collected from 31 mice ($n = 18$ in LP, 4 in LGN, and 9 in SC). For recordings in cerebellum (Ce), data were collected from one mouse with three different penetrations. All data were acquired with Neuropixels probes (Jun et al. 2017) with 30-kHz sampling rate and recorded with the Open Ephys GUI (Siegle et al. 2017). A 300-Hz high-pass filter was present in the Neuropixels probe, and another 300-Hz high-pass filter (3rd-order Butterworth) was applied offline before spike sorting.

Histology. For recordings in visual cortex and HP, the probe location was confirmed by clearing brains with dichloromethane and dibenzylether (<https://idisco.info/idisco-protocol/>) and imaging with optical projection tomography (OPT; Supplementary Fig. S1A). OPT showed most recordings from HP were from CA1 region given our probe insertion location and depth. To assign probes to specific visual areas, we overlaid an image of the brain surface obtained during the recording session on images obtained from intrinsic signal imaging, using the vasculature for registration (Supplementary Fig. S1B). For recordings in other brain areas, recording location was subsequently verified by identifying the DiI fluorescence in sectioned brain tissue (Supplementary Fig. S1, *C*–*F*).

Data preprocessing. In all experiments, spike times and waveforms were automatically extracted from the raw data using Kilosort (Pachitariu et al. 2016). Kilosort is a spike-sorting algorithm developed for electrophysiological data re-

corded by hundreds of channels simultaneously. It implements an integrated template matching framework for detecting and clustering spikes, rather than clustering based on spike features, which is commonly used by other spike-sorting techniques. The outputs of Kilosort were loaded into phy (Rossant et al. 2016) for manual refinement, which consisted of merging and splitting clusters, as well as marking non-neural clusters as “noise.” Noise units were identified by their abnormal waveform shape, as well as distinct cyclical patterns in the autocorrelogram. Merges were made when the cross-correlogram between two units dropped to near zero at a 1 to 2 ms temporal offset, indicating the presence of a refractory period. Splits were made when the spikes for one unit displayed multiple readily separable clusters when projected in principal component analysis (PCA) space. In this case, a boundary was manually drawn around one of the clusters, thereby splitting the unit in two. If the resulting cross-correlogram showed no evidence of a refractory period, the split was maintained; otherwise, the split was reverted. We then used a set of heuristic rules based on the features of waveforms to remove abnormal waveforms [the parameters used for this purpose were peak-to-trough (PT) ratio <0.99 and recovery slope <0]. No further constraints were imposed.

Waveforms for each unit were extracted from the raw data by slicing around the trough time (pre-trough points = 20 samples, total waveform size = 82 samples, with 30-kHz sampling rate). For each unit, the mean waveform was calculated from bootstrapped waveforms (number of spikes = 100; number of repetitions = 100) from all spikes. If the number of spikes for a given unit was smaller than 100, then all the waveforms were used to calculate the mean waveform. Mean waveforms for experiments with optotagging were calculated only on waveforms before the light stimulation period, to avoid artifacts in waveform traces caused by light.

Optotagging

Optotagging was performed in a subset of the visual cortex experiments described above, using Pvalb-Cre \times Ai32 (ChR2 reporter) mice. In each experiment, a 200- μm -diameter bare fiber-optic cable (Thorlabs) connected to a 465-nm light-emitting diode (LED; Plexon) was aligned with the center of the cranial window such that it illuminated a surface area of $\sim 20 \text{ mm}^2$. Stimulus trains were delivered with a Cyclops LED driver and consisted of 2.5-ms square-wave pulses at 10 Hz, individual square-wave pulses lasting 5 or 10 ms, or 1-s raised cosine ramps. Peak light power varied from 0.1 to 10 mW on a given trial. Each stimulus condition (pulse type \times power) was repeated 120 times. Light artifacts were visible on all channels but were readily separable from actual spikes based on timing relative to the stimulus and waveform shape.

Analysis

Waveform feature extraction. To classify cell types, we first extracted features from the extracellular waveform. With high-density Neuropixels probes, we recorded extracellular waveforms of a single unit from multiple sites. We define the recording site with highest amplitude (absolute difference between trough and peak of an extracellular waveform) as the site closest to neuron soma, and the extracellular waveform recorded here is our single-channel waveform. To take advantage

of signals detected by multiple sites, we consider the profile of extracellular waveforms of a single sorted unit recorded from multiple adjacent recording sites as a multichannel waveform. The probe was inserted along the dorsal-ventral axis of the brain. Because the Neuropixels probe has two recording sites at each depth, we used only the side of the probe with higher waveform amplitude to calculate the multichannel waveform. The distance between sites is approximated by their vertical spacing (20 μm). The horizontal spacing is ignored here, but it could potentially contribute to differences between adjacent sites.

For single-channel (1-channel) waveforms, we extracted five features: amplitude, duration, PT ratio, repolarization slope, and recovery slope (Fig. 2B). Waveform peak was defined by the maximum point of extracellular waveform. Trough was defined by the minimum point. Amplitude was defined by the absolute difference between peak and trough. Duration was defined by the time between waveform trough and peak. This feature is commonly used to separate FS neurons from RS neurons (McCormick et al. 1985; Mitchell et al. 2007; Niel and Stryker 2008; Swadlow 2003). PT ratio was determined by the absolute amplitude of peak divided by absolute amplitude of trough relative to 0. The repolarization slope was defined by fitting a regression line to the first 30 μs from trough to peak. The recovery slope was defined by fitting a regression line to the first 30 μs from peak to tail.

For multichannel waveforms (Fig. 3A), we extracted three additional features in the space domain for classification: spread along the probe and the inverse of propagation velocity above and below soma along the probe. The spread of a unit was defined by the distribution of its waveform amplitude. If we plot amplitude against recording site distance relative to soma, we get a curve with peak at 0 (Fig. 3C). We defined the range with amplitude above 12% of the maximum amplitude as the spread of a unit along the probe. The multichannel waveform has information in both time and space dimension for signal propagation velocity estimation. Because the time difference between the trough of adjacent sites could be 0, to avoid infinite numbers, we calculated the inverse of velocity (ms/mm) instead by fitting a regression line to the time of waveform trough at different sites against the distance of the sites relative to soma (Buzsáki and Kandel 1998). All waveforms and features are available at https://github.com/jiaxx/waveform_classification.

Random forest classification. To classify the brain structure each unit belongs to with extracellular waveforms, we used random forest classification. This supervised learning algorithm provides the contribution of each feature to classification accuracy. In addition, because the accuracy of random forest classification is averaged across many estimators, it is less likely to overfit the data than a decision tree. The two hyperparameters for our random forest classifier, the number of estimators and the depth of the decision trees, were estimated via grid search implemented in Scikit-Learn (Pedregosa et al. 2011) using fivefold cross-validation for different feature sets. Because classifier performances for different feature sets plateaued above certain hyperparameter values (see Supplemental Fig. S4), we chose a fixed set of hyperparameters that reached plateau performance (maximum tree depth = 14 and number of estimators = 80) for all feature sets rather than fine-tuning hyperparameters for individual set of features.

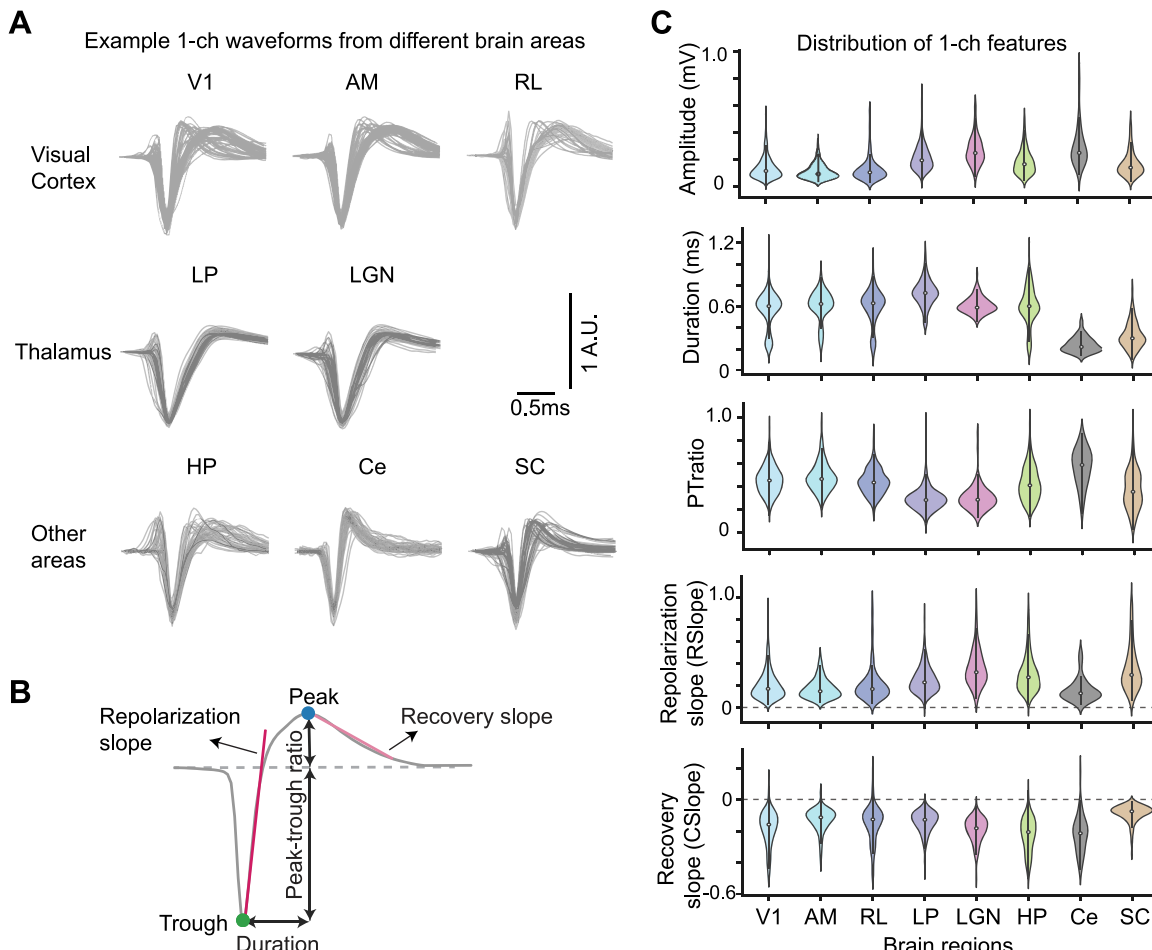


Fig. 2. Spike waveform features extracted from single-channel waveforms. *A*: example normalized mean waveforms for single units from 8 different brain areas (gray lines show 50 randomly sampled single units for each area; waveforms are normalized by amplitude). 1-ch, Single-channel; Ce, cerebellum; HP, hippocampus; LGN, lateral geniculate nucleus; LP, lateral posterior nucleus; SC, superior colliculus; V1, AM, and RL, areas of visual cortex. *B*: illustration of features extracted from single-channel waveform (green and blue circles indicate trough and peak, respectively). Amplitude is the absolute difference between trough and peak. Duration is the time between trough and peak. Peak-to-trough ratio (PT ratio) is the ratio between amplitudes of peak and trough. Red lines show slopes for repolarization and recovery. *C*: distributions of single-channel features in different brain regions. Violin plots show feature distributions estimated with a kernel density function. The white dot indicates median, the thin line shows 95% bootstrapped confidence interval, and colors correspond to different areas (V1, $n = 1,111$; AM, $n = 234$; RL, $n = 264$; HP, $n = 369$; LP, $n = 485$; LGN, $n = 106$; SC, $n = 171$; Ce, $n = 78$ units). The ANOVA one-way test is applied to each feature across areas. All tests showed $P << 0.001$. Statistics of post hoc pairwise comparison are available in Supplemental Fig. S2.

All classifications were performed with a fivefold cross-validation where the classifier was trained on a subset of the data (80%), and then the classifier's performance is evaluated on the held-out test data (20%). Classification accuracy was determined by the out-of-bag score, which is estimated on the basis of the prediction accuracy of data left out in each fit of the decision tree (estimator) on bootstrapped subsamples. Because there were significantly more units in the visual cortex than other brain regions, we subsampled 77 units (determined by $n = 78$ units in cerebellum) randomly from all regions to balance the size of the data set from different brain regions to minimize the influence from underlying class distribution on accuracy. The confusion matrix was computed by comparing predicted classes with true classes for 100 subsampled data sets under 100 random initial states. The trend of classification accuracy compared across different feature sets is not different between matched-sample classification and unbalanced-sample classification.

K-means clustering. We applied *k*-means algorithm to determine cell clusters within visual cortex. The *k*-means method

is a widely used clustering technique that seeks to find centroids that minimize the average Euclidian distance between points in the same cluster to the centroid. However, one of its drawbacks is the requirement for the number of clusters, K , to be specified before the algorithm is applied. We applied two methods in estimating number of clusters in visual cortex (see Supplemental Fig. S5). One method is the standard elbow method, which estimates the percentage of variance explained for a given number of K . The number of K is estimated at the point when the curve turns to plateau. Another method estimates the data distribution for a given K , calculated by a density function $f(K)$ (Pham et al. 2005). The value of $f(K)$ is the ratio of the real distortion to the estimated distortion. When the data are uniformly distributed, the value of $f(K)$ is 1. When there are areas of concentration in the data distribution, the value of $f(K)$ decreases. Therefore, the number of K clusters is determined by finding the minimum value of $f(K)$. Combining estimation of K using the above two methods, we decided on K and applied *k*-means to data with an appropriate number of K for 1,000 times with random initial values.

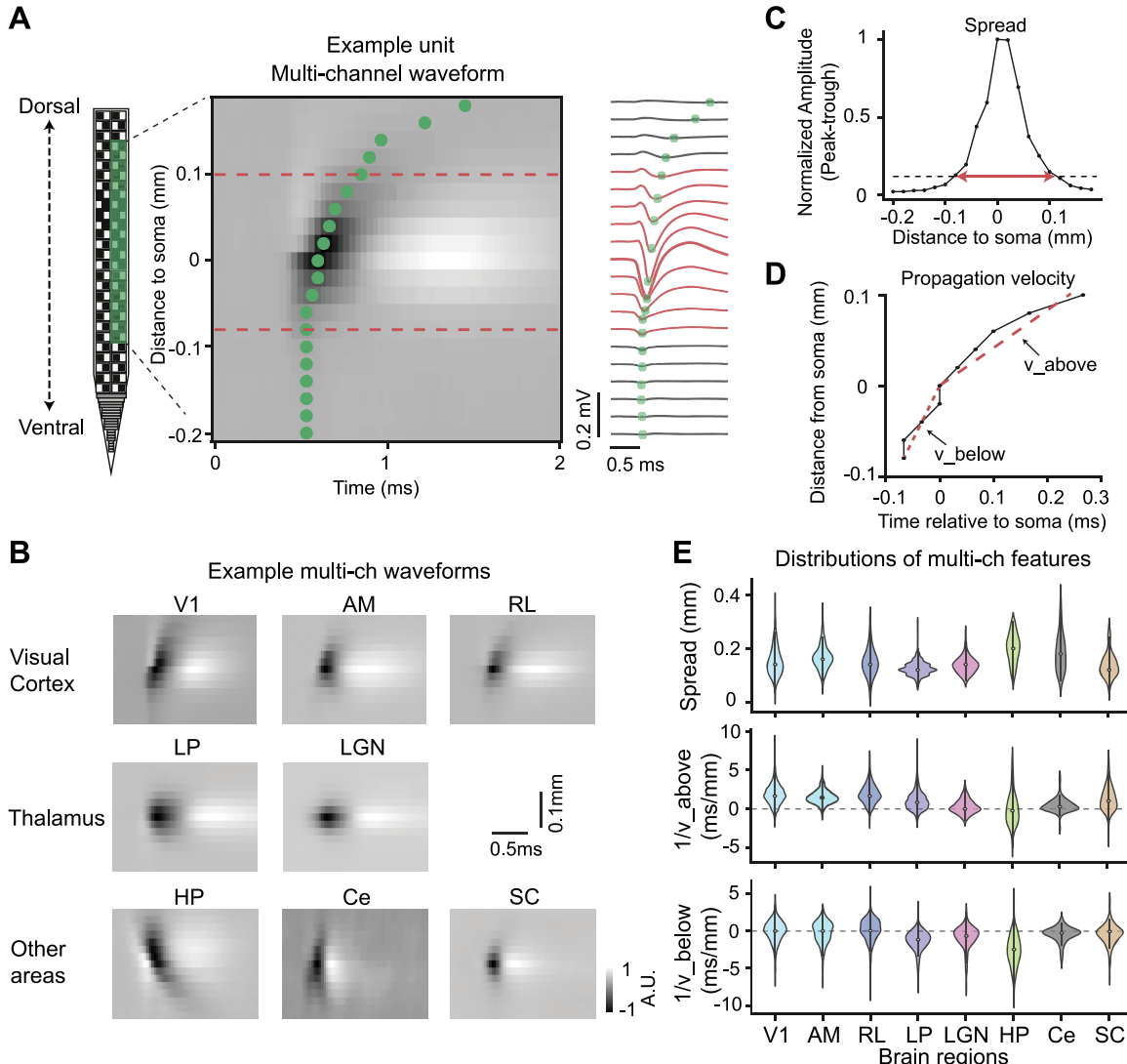


Fig. 3. Features extracted from multichannel waveforms. **A:** illustration of multichannel extracellular waveform of an example unit. The probe is inserted along the dorsal-ventral axis of the brain and has two parallel columns of recording sites at each depth; for each unit, we used waveforms measured on one column of the probe (see METHODS). The multichannel waveform includes the channel with the largest amplitude and 10 channels both above and below. In the heatmap, each row represents the spike from one recording site over time; these same data are plotted as a time series at right. Green dots indicate waveform trough at each recording site. Red dashed line indicates the spread of detectable extracellular waveform along the probe, defined in **C**. **B:** example multichannel waveforms from different brain areas showing diverse profiles (see additional example waveforms in Supplemental Fig. S3). Ce, cerebellum; HP, hippocampus; LGN, lateral geniculate nucleus; LP, lateral posterior nucleus; SC, superior colliculus; V1, AM, and RL, areas of visual cortex. **C:** amplitude of the example unit as a function of recording distance to soma. The spread of the waveform along the probe is defined as the distance over which the spike amplitude is larger than 12% of the maximum amplitude. For the example unit, channels within the defined spread are colored in red in **A**. **D:** propagation trajectory along the probe for the example unit. For each electrode location (y -axis; $y = 0$ indicates potential soma location), the time of the waveform trough is plotted on the x -axis. Velocity above (v_{above}) and below (v_{below}) soma are separately estimated by linear regression (red dashed lines). **E:** distributions of features extracted from multichannel waveforms in different brain regions: spread along probe (**top**), inverse of velocity above soma ($1/v_{\text{above}}$; **middle**), and inverse of velocity below soma ($1/v_{\text{below}}$; **bottom**). The ANOVA one-way test is applied to each feature across areas. All tests showed $P << 0.001$. Statistics of post hoc pairwise comparison are available in Supplemental Fig. S2.

***t*-Distributed stochastic neighbor embedding.** *t*-Distributed stochastic neighbor embedding (*t*-SNE) is a nonlinear dimensionality reduction for the visualization of high-dimensional data sets. We used Laures van der Maaten's method (van der Maaten and Hinton 2008) to visualize all units in two-dimensional space with different features. The purpose is to visualize whether units from same structure are mapped to similar regions with a given feature set (Fig. 4A). We also visualized unlabeled data to check whether there are any clusters in units with a given feature set.

Classification of optotagged neurons. We developed a new method to determine optotagged cells on the basis of their

response to different light stimulation patterns. Response post-stimulus time histograms (bin size = 1 ms) to different light patterns (individual square-wave pulses lasting 5 or 10 ms, or 1-s raised cosine ramps) were concatenated to form a response vector for each unit, which resulted in an n_{units} (neurons) by n_{feature} (time) matrix. We then normalized the matrix and applied PCA to reduce the dimensionality while keeping 90% variance. *K*-means was applied to the normalized data for 1,000 times with random initial value. This process was repeated 100 times to generate a probability matrix with each pixel value indicating the probability of a pair of units belonging to the same cluster. Hierarchical clustering was applied to

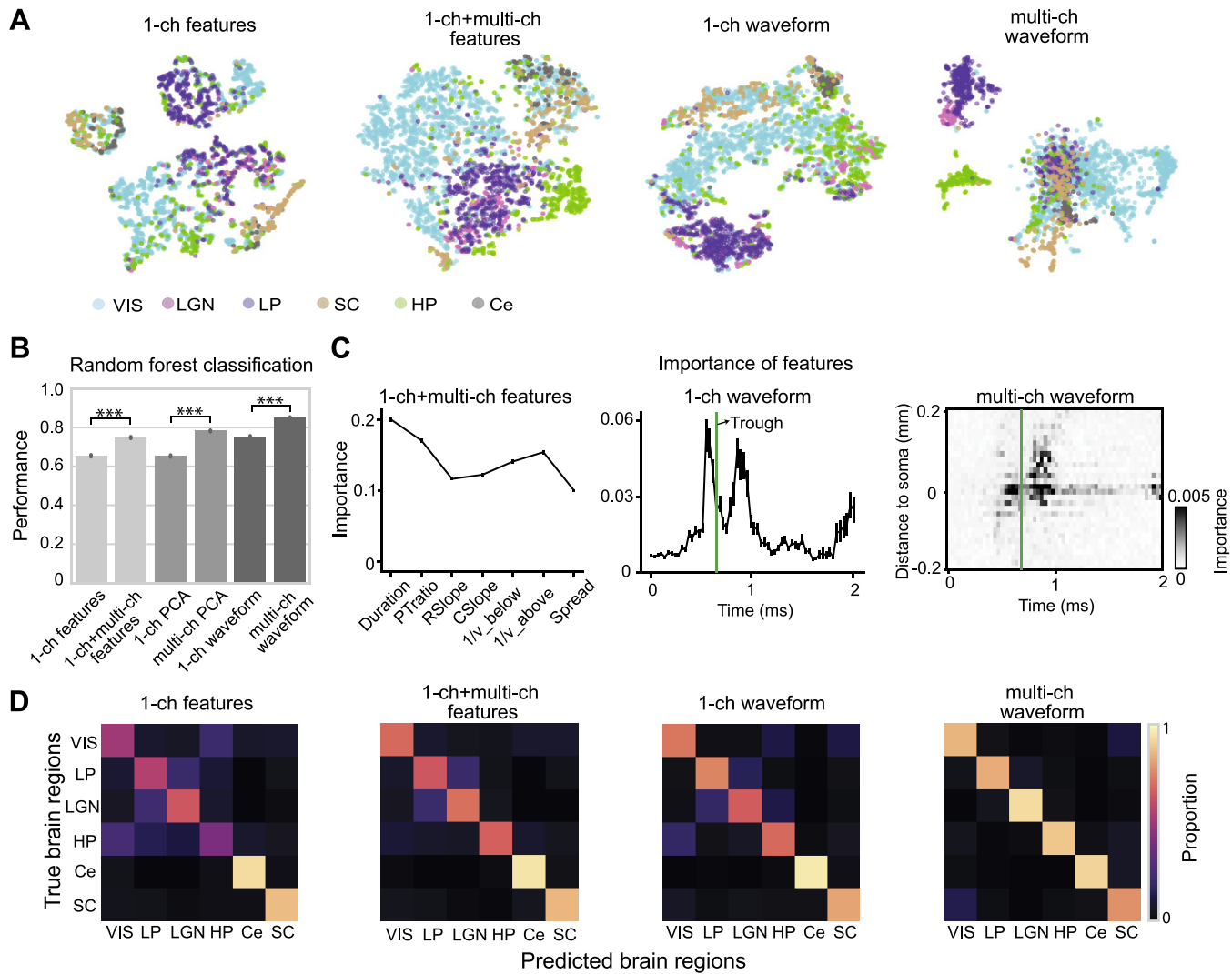


Fig. 4. Classification of unit brain region using extracellular waveform features. **A:** *t*-distributed stochastic neighbor embedding (t-SNE) visualization of units from distinct brain regions based on different waveform features. Each dot corresponds to one unit, and brain regions are color coded ($n = 2,818$ units). From left, t-SNE representations are computed with features extracted from 1-channel (1-ch) waveform, features extracted from both 1-ch and multichannel (multi-ch) waveforms, a 1-ch waveform, and a multi-ch waveform. Ce, cerebellum; HP, hippocampus; LGN, lateral geniculate nucleus; LP, lateral posterior nucleus; SC, superior colliculus; V1S, visual cortex. **B:** performance (out-of-bag score) classifying unit brain region based on 1-ch features alone ($n_{\text{feature}} = 4$), all extracted features ($n_{\text{feature}} = 7$), principal component analysis-reduced (90% variance retained) waveform features (1-ch, $n_{\text{feature}} = 5$; multi-ch, $n_{\text{feature}} = 52$), and the whole waveform (1-ch, $n_{\text{feature}} = 60$; multi-ch, $n_{\text{feature}} = 1,800$). *** $P < 0.001$, statistical comparisons between the performance of 1-ch and multi-ch performed with Student's *t*-test. Error bars are computed over different random samples without replacement ($n = 100$). **C:** importance of features calculated with random forest classification: importance of extracted features ($n_{\text{feature}} = 7$; left), importance of 1-ch waveform ($n_{\text{feature}} = 60$; middle), and importance of multi-ch waveform ($n_{\text{feature}} = 1,800$; right). **D:** confusion matrix of random forest prediction vs. true brain regions for different feature sets. Color indicates proportion of units. The average of the diagonals corresponds to mean performance in **B**.

the probability matrix to determine different clusters. The cluster of units with responses that tightly follow the light pattern was defined as optotagged cells. The rest were determined as non-optotagged units. These results were confirmed with labeling based on changes in firing rate and the significance of those changes (Hangya et al. 2015).

Current source density. For estimation of unit depth within the cortex, we performed current source density (CSD) analysis by computing the average evoked (stimulus locked) local field potential at each site, smoothing these signals across sites, and then calculating the second spatial derivative (Smith et al. 2013; Stoelzel et al. 2009). For spike-triggered CSD, we applied the same metric to the average multichannel waveform across units (Bereshpolova et al. 2007).

RESULTS

We analyzed extracellular action potentials recorded from 43 adult mice using Neuropixels probes. In each recording session, the mouse was awake and head-fixed on a wheel to allow free running behavior (Fig. 1A). After spike sorting with semiautomated algorithms (Pachitariu et al. 2016; Rossant et al. 2016), followed by manual quality control, we recovered 2,818 single units (see METHODS). The units were stable over the recording session, and the average refractory period violations were low ($0.88 \pm 0.03\%$ of total spikes per unit) (Supplemental Fig. S1). These units were recorded from eight brain regions: primary visual cortex V1 (V1Sp; 1,111 units), cortical visual area AM (V1Sam; 234 units), cortical visual area RL (V1Srl; 264 units), hippocampus (HP; 369 units, mostly dorsal

CA1; see METHODS), lateral geniculate nucleus (LGN; 106 units), lateral posterior nucleus (LP; 485 units), superior colliculus (SC; 171 units), and cerebellum (Ce; 78 units) (Fig. 2A). On average, we recorded 64 ± 6 units in cortex per probe insertion. To verify the brain regions recorded by each probe, we used post hoc histology, imaging, and annotation using the Allen Mouse Common Coordinate Framework (Supplementary Fig. S1). Subregions of visual cortex (VISp, VISam, VISrl) were determined by functional retinotopic mapping before the experiment, and these maps were used to guide probe insertion. Thus, for each recording, we could label each sorted unit with its brain region. The action potential waveforms analyzed in this report refer to the mean waveform for each sorted unit, which is calculated by taking a bootstrapped average (number of spikes = 100; number of repetitions = 100) from all spikes aligned by their trough (see METHODS). We defined the single-channel waveform for a given unit as the mean action potential recorded on the channel with the largest amplitude; often this channel is assumed to be closest to the soma (Buzsáki and Kandel 1998), and we follow that convention here.

Comparison of Single-Channel Waveforms from Different Brain Regions

We first investigated whether neurons in different brain regions have distinct single-channel (1-channel) waveform profiles (Fig. 2A; each line is the mean waveform for 1 unit, normalized by amplitude). Units in the visual cortex and HP show a diversity of 1-channel waveform shapes, including both narrow and wide spikes; in contrast, 1-channel waveforms from the Ce are more consistently narrow, whereas thalamic cells are more consistently broad (Fig. 2A). To quantitatively compare spikes, we extracted a series of features from the 1-channel waveforms, including amplitude, spike duration (Barthó et al. 2004; Mitchell et al. 2007), PT ratio (Andermann et al. 2004; Hasenstaub et al. 2005), repolarization slope after trough (Niell and Stryker 2008), and recovery slope after peak (Fig. 2B). The distribution of features from different brain regions is plotted in Fig. 2C (Supplemental Fig. S2 shows mean and confidence intervals). Previous studies have used these parameters, particularly spike duration, to separate extracellular waveforms into two classes labeled fast spiking (FS) and regular spiking (RS) (Mitchell et al. 2007; Niell and Stryker 2008). We observed that in the neocortex and HP, the distributions of spike duration were bimodal, indicating the presence FS and RS subpopulations in these regions (Fig. 2C).

In general, we found that 1-channel waveform features were significantly different across brain areas (see Supplemental Fig. S2 for statistical tests of all area-by-area comparisons). Post hoc analysis using the paired *t*-test with Bonferroni correction indicated that cortical neurons had smaller spike amplitudes compared with the subcortical neuron types we recorded. The spike duration of units recorded in visual cortex and hippocampus were largely similar (all *P* values are reported in Supplemental Fig. S2, where “n.s.” indicates *P* > 0.05 with Bonferroni correction) but differed from units recorded in the SC, Ce, and LP. Cortical neurons had larger PT ratio compared with units in thalamus. Units in LP had the longest duration (0.73 ± 0.12 ms, mean \pm SD) and smallest PT ratio (0.29 ± 0.09) compared with units from other

brain regions. Waveforms recorded from SC (mean duration = 0.33 ± 0.12 ms) and Ce (mean duration = 0.24 ± 0.07 ms) were significantly narrower than other brain regions (*P* << 0.01). The above results reflected differences of single-channel waveforms among neurons recorded in different brain regions. Next, we investigated whether additional differences could be revealed by analyzing multichannel waveforms.

Distinct Multichannel Waveforms Measured in Different Brain Regions

Compared with traditional single-electrode and multielectrode arrays, one advantage of the Neuropixels probe is the relatively dense arrangement of recording sites. Signals from a single unit can be detected on many recording channels (see Fig. 3f in Jun et al. 2017), providing an additional dimension (space) to characterize cell type-specific spike properties. We defined a multichannel spike waveform to include the maximum spike channel (closest to soma) and 10 additional channels above and below the peak channel, spanning ± 200 μ m along the probe. This multichannel spike waveform can be visualized as a heatmap or as a series of voltage traces for each electrode channel (Fig. 3A). Figure 3B shows example multichannel waveforms from eight different brain regions (with additional single-unit examples shown in Supplemental Fig. S3). The spatial extent of spike waveforms varied across areas. In addition, we noticed that the trough of many spike waveforms appeared to propagate along the linear probe (see visual cortical and HP units in Fig. 3, A and B, and Supplemental Fig. S3) (Bereshpolova et al. 2007; Buzsáki and Kandel 1998).

To quantify and compare these spatiotemporal spike properties, we next computed several features designed to capture the multichannel spread and propagation velocity. We defined the spread as the distance spanning the contiguous set of electrode sites with spike amplitude larger than 12% of the peak channel (Fig. 3C). To characterize spike propagation, we computed the time of the spike trough at each channel within the spread of the spike as a function of channel distance relative to soma (channel with peak amplitude). As shown in Fig. 3D, the propagation velocity can be computed as the slope of the trough distance vs. trough time. To avoid infinite values caused by the waveform trough occurring on adjacent sites at the same time for some waveforms, we computed the inverse of the velocity separately for the spike propagating above and below the cell body location.

The distributions of spread and propagation metrics showed consistent differences across brain regions (Fig. 3E; ANOVA 1-way test: all *P* << 0.001). Post hoc pairwise comparisons using the paired *t*-test with Bonferroni correction showed that the spread of units in LP, LGN, and SC is smaller than in other regions (*P* < 0.05; Supplemental Fig. S3). Inverse of velocity was indistinguishable among different visual cortical areas (among V1, AM, RL; *P* > 0.05). The inverse of velocity above soma was significantly positive in all visual cortical areas (mean 1.83 ± 0.03 ms/mm; 1-sample *t*-test, *P* << 0.001), indicating a bias for propagating waves dorsally toward the pia (with mean velocity = 0.54 mm/ms). In contrast, in the dorsal HP, where cells are oriented such that the apical dendrites point ventrally, the inverse propagation velocity below soma was significantly negative (-2.60 ± 0.11 ms/mm; 1-sample *t*-test, *P* << 0.001), indicating a bias for propagating spike wave-

forms toward the stratum radiatum in CA1 (mean velocity = 0.38 mm/ms). Further analysis of propagation profiles is explored in *Spike Waveform Clusters Within Visual Cortex and Backpropagating Action Potentials in Cortex and Hippocampus* (see Fig. 6 and Supplemental Fig. S9).

Brain Region Classification Based on Extracellular Waveforms

Because extracellular waveforms showed significantly different feature distributions across brain areas (Figs. 2 and 3, Supplemental Fig. S2), we next tested whether these features could be used to predict which brain region each unit resides in and whether the multichannel waveform can provide additional information beyond the 1-channel waveform for classifying unit brain regions. We did not include waveform amplitude as a feature for classification because it is strongly affected by the relative distance of the electrode to soma (Gold et al. 2006; Weir et al. 2015). Given the similarity of the waveforms recorded in the three visual cortical areas (VIS: VISp, VISam, VISrl), we grouped all the units from visual cortex in the following analysis ($n = 1,609$ units).

To visualize whether there is any clustering of units in a lower dimensional space with different waveform feature sets, we first used t-SNE (van der Maaten and Hinton 2008), which is a nonlinear dimensionality reduction technique to embed high-dimensional data in a low-dimensional space for visualization (Fig. 4A). Each dot represents one sorted unit, and the color indicates the source brain region labeled by histology. Embedding with features extracted from 1-channel waveforms ($n_feature = 4$) was comparatively worse in forming clusters of brain regions; in contrast, features extracted from multichannel waveforms showed better separation among brain regions with $n_feature = 7$. Use of the full single-channel waveform ($n_feature = 60$) does not separate HP from cortical cells, whereas use of the full multichannel waveform pushes HP and thalamus far away from other regions. This visualization suggests multichannel features contain more information to distinguish brain regions than single-channel waveforms, but this nonlinear embedding is hard to interpret quantitatively.

To quantitatively assess area classification from high-density recordings, we trained random forest classifiers to use waveform features to predict the brain region to which each unit belongs. We chose random forest classification because this method minimizes overfitting to training data and makes it possible to assess the contribution of each feature to classification accuracy. To remove potential classification bias that could result from an imbalanced number of units from different brain regions, we subsampled 77 units (without replacement) randomly from each of six brain regions [VIS (including areas VISp, VISam, VISrl) LGN, LP, SC, HP, and Ce]. Thus, for a six-way classification, there is a 0.17 chance probability for classifiers trained to predict brain regions. Hyperparameters for random forest were chosen using grid search with fivefold cross-validation (see METHODS for details; Supplemental Fig. S4). We compared brain region classification based on different sets of waveform features including 1) extracted features (e.g., duration, PT ratio, inverse propagation velocity), 2) PCA on 1-channel or multichannel waveform (90% retained variance), and 3) the entire 1-channel or multichannel spike waveform (Fig. 4B). Classification performance from all feature sets

was significantly above chance, with the highest equal to $85.1 \pm 1.6\%$ for the multichannel waveform (SD across 100 different subsamples). Overall, classification performance was improved by using features beyond the traditional 1-channel features (*t*-test, $P < 0.001$), indicating that the spatiotemporal profile of the spike waveforms carries additional relevant information for clustering cell types from different brain regions. Notably, if the additional features from the multichannel waveform did not contain useful information for separating neurons from different brain regions, adding these features would not increase performance.

One advantage of random forest classification is its ability to analyze the importance of the features for classification accuracy (Fig. 4C). Importance in this context is defined as the total decrease in node Gini impurity (weighted by the proportion of samples reaching that node) averaged over all the ensembles (Breiman et al. 1984). From our extracted features, the spike duration and PT ratio were the most important features, and spread was the least important (Fig. 4C, left). For data points in the 1-channel waveform, the samples just before the trough and around the peak are the most important (Fig. 4C, middle). For the multichannel waveform, the samples on the peak channel were important (distance to soma = 0 μm), but there was also a clear contribution of the waveform captured on the spatially adjacent electrode sites within 100–200 μm of the soma location, with propagation before and after the trough (Fig. 4C, right). This importance map of multichannel waveforms clearly showed which features in time and space were most relevant for distinguishing neurons from different brain regions and could be used as guidance for future feature extraction.

To investigate the misclassification errors that led to imperfect performance with these classifiers, we plotted confusion matrices for different classifiers (with corresponding performance in Fig. 4B) to show the predicted vs. true brain regions of subsampled units ($n = 462$ units in total, for 77 random samples from each area; Fig. 4D). Ce and SC are clearly distinctive from other brain regions for all classifiers. Adding features from the multichannel waveform helped distinguish HP and thalamus from other brain regions. Interestingly, thalamic units in the LGN could be differentiated from those in the neighboring LP thalamic nucleus by using the multichannel waveform, potentially based on their duration and spread (Figs. 2 and 3). Classification without subsampling resulted in higher performance but a similar trend compared across different feature sets (data not shown). Thus the classification results qualitatively agree with unsupervised embedding and together suggest that the multichannel spike waveform profile carries additional information useful for identifying cell classes residing in distinct brain regions.

Spike Waveform Clusters Within Visual Cortex

We next examined whether the multichannel waveform can assist the classification of cell types within a brain region. For this analysis, we focused on waveform types in the visual cortex. The population of visual cortical neurons have a bimodal distribution of spike durations (Fig. 2C), suggesting the presence of at least two neuron types (FS and RS). To determine whether multichannel spike features can identify further waveform types, we applied *k*-means clustering to the cortical cells. Using the combined 1-channel and multichannel features,

we estimated three waveform clusters using the conventional elbow method and a k -cluster density function (see METHODS and Supplemental Fig. S5). We visualized these clusters in a two-dimensional space using a t-SNE plot (Fig. 5A) with colors representing k -means cluster labels. One of the clusters corresponds to the FS waveform, which includes units with comparatively short-duration spikes (Fig. 5B). In addition to the FS cluster, which accounted for 19.6% of total units, we identified two regular spiking waveform clusters that we label as RS1 and

RS2; these comprise 59.6% and 20.8% of the visual cortex units, respectively. When only the 1-channel waveform was considered, the RS1 and RS2 waveforms looked very similar in their duration and PT ratio (Fig. 5B). However, the spatiotemporal structure of the multichannel spike waveforms is strikingly different between the RS1 and RS2 clusters (Fig. 5C). The average RS1 waveform propagates from below the cell body upward along the probe toward the dorsal surface of the brain; in contrast, the average RS2 waveform propagates a

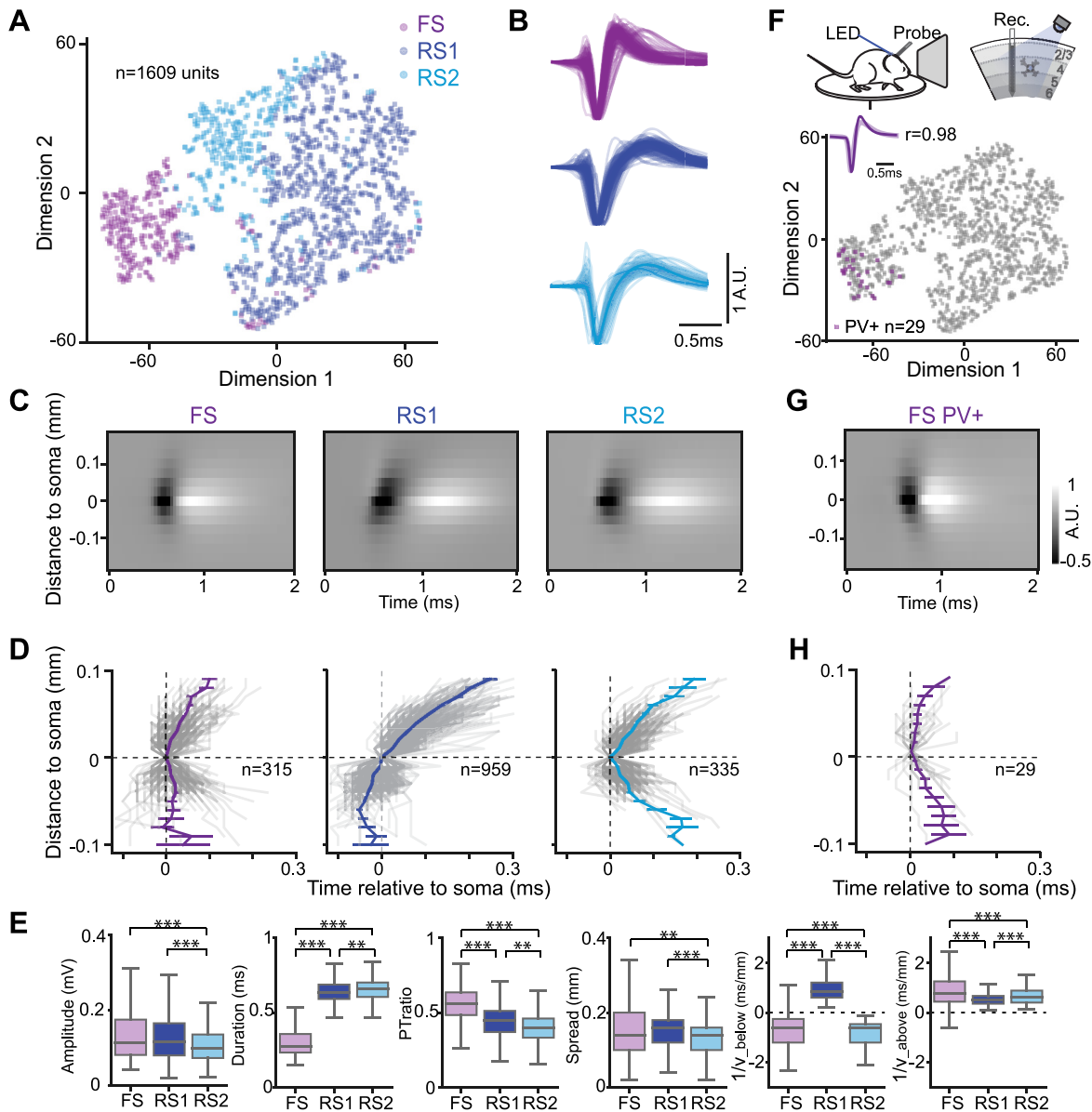


Fig. 5. Unsupervised clustering of extracellular waveforms in visual cortex. **A:** t-distributed stochastic neighbor embedding (t-SNE) for all units in visual cortex ($n = 1,609$ units from 11 mice) based on features extracted from 1-channel and multichannel waveforms. Units are colored according to k -means clustering into 3 groups: fast-spiking neurons (FS; $n = 315$), regular-spiking neurons type 1 (RS1; $n = 959$), and regular-spiking neurons type 2 (RS2; $n = 335$). **B:** normalized example waveforms for units from different clusters (each trace is the mean waveform of a unit; $n = 50$ sampled units for each cluster). **C:** average multichannel waveforms for different clusters. **D:** spike propagation trajectory from soma for all units in each cluster. Gray lines indicate individual units and colored lines indicate means \pm SE. **E:** boxplot of features for different subclasses in visual cortex. The line dividing each box indicates the median of distribution, and the box represents the middle 50% of scores for the group. $**P < 0.01$; $***P < 0.001$, pairwise comparisons computed with Bonferroni-corrected t -test. **F:** optotagging of parvalbumin-expressing (PV+) cells in the visual cortex with Pvalb-Cre;Ai32(ChR2) mice ($n = 4$ insertions from 2 mice). *Top:* an illustration of the experimental setup for optotagging experiments. Probes are inserted vertically in the visual cortex. Blue LED light illuminated the surface of the exposed cortex (peak power = 10 mW). *Bottom:* the t-SNE representation from A with color-labeled PV+ cells ($n = 29$). The average 1-ch waveform from PV+ cells is overlaid on the average 1-ch waveform FS cluster with Pearson correlation $r = 0.98$. Rec., recording. **G:** averaged multichannel waveform for PV+ cells. **H:** spike propagation trajectories for PV+ cells. Error bars indicate SE. A.U., arbitrary units.

shorter distance, symmetrically around soma (Fig. 5D). The propagation profile for the FS cluster is also symmetric around the cell body but is relatively flat with a median slope value not different from zero.

Overall, the three clusters showed significant differences in several 1-channel and multichannel features (Fig. 5E). FS neurons had significantly shorter duration (Bonferroni-corrected *t*-test, $P << 0.001$), larger PT ratio ($P << 0.001$), and relatively fast bidirectional propagation from soma. Comparison of the two RS subclasses showed the total spread of RS1 units (median = 0.16 mm) was broader than that of RS2 units (median = 0.14; Bonferroni-corrected *t*-test, $P = 9.77\text{E-}7$), the amplitude of RS1 units (median = 0.115) was larger than that of RS2 units (median = 0.098; Bonferroni-corrected *t*-test, $P = 7.67\text{E-}7$), and the PT ratio of RS1 units (median = 0.45) was larger than that of RS2 units (median = 0.40; Bonferroni-corrected *t*-test, $P = 1.23\text{E-}13$). More strikingly, the velocity of waveform propagation above (0.45 ± 0.01 mm/ms; Bonferroni-corrected $P << 0.001$ compared with channel-shuffled null distribution) and below (1.25 ± 0.02 mm/ms; Bonferroni-corrected $P << 0.001$) the cell body were both positive in RS1 units, indicating a unidirectional active spike propagation, likely starting at the spike initiation zone and propagating upward to the cell body and along the apical dendrites of pyramidal neurons. On the contrary, the velocity above soma was positive for RS2 units (0.59 ± 0.01 mm/ms; $P << 0.001$), but the velocity below soma was negative (-0.59 ± 0.01 mm/ms), indicating a bidirectional propagation profile in RS2 cells. To determine if the velocity below soma might by itself differentiate RS1 from RS2, we performed a test for bimodality in the distribution of this metric, which proved significant (Hartigan's dip test: $D = 0.049$, $P < 2.2\text{E-}16$).

We considered the possibility that the RS1 and RS2 unit clusters might be caused by variation in the angle of probe insertion into the cortex rather than reflecting distinct cell classes. If this were the case, we might observe strong biases in the fraction of RS1 vs. RS2 units across individual probe insertions. In contrast to this prediction, we found that all cortical probe insertions included a relatively consistent proportion of units falling into both the RS1 and RS2 clusters (per probe, $58.7 \pm 1.9\%$ of units were classified as RS1 and $21.2 \pm 2.1\%$ as RS2; $n = 25$ probes from 11 mice). Moreover, we found no systematic relationship between the length of spike backpropagation on a given probe (an indicator of probe alignment with pyramidal neuron apical dendrites) and the proportion of RS1 and RS2 units (Pearson correlation = 0.27 and $P = 0.19$; Supplemental Fig. S6). In addition, the backpropagation profile of RS1 units is stable throughout the recording session regardless of changes in running or stationary behavioral states (Supplemental Fig. S7), consistent with the previous observation (Bereshpolova et al. 2007).

To test whether the waveform clusters we identified via *k*-means clustering were consistent with known genetically defined cell types, we performed optotagging experiments in transgenic mice expressing channelrhodopsin in PV+ inhibitory interneurons in the cortex [Pvalb-IRES-Cre; Ai32(ChR2); Fig. 5F]. We used a fiber-coupled LED to illuminate the brain surface with both pulse and ramping optostimulation patterns to induce a rich response pattern that was used to identify optotagged neurons whose activity profile closely followed the stimulus light pattern (see METHODS; Supplemental Fig. S8). We

optotagged 29 PV+ neurons (4 insertions from 2 mice), and each of these units was classified as FS based on hierarchical clustering (see METHODS). These units clearly fall into the FS cluster shown on the t-SNE plot (Fig. 5F; 100% PV+ are FS). The PV+ optotagged neurons have short-duration spikes, and their multichannel waveform does not show evidence of unidirectional action potential backpropagation (Fig. 5, G and H). Thus genetically identified PV+ visual cortical neurons are of the FS waveform type.

Backpropagating Action Potentials in Cortex and Hippocampus

A previous study showed that backpropagating action potentials in layer 5 pyramidal neurons in rabbit visual cortex are associated with a traveling wave of current sinks and sources along the apical dendrite (Bereshpolova et al. 2007). To determine whether the three waveform types we identified in visual cortex (VIS-FS, VIS-RS1, and VIS-RS2) have distinct patterns of current sinks and sources, we computed the spike-triggered current source density (sCSD; see METHODS) profile for each type (Fig. 6A). Because sCSD is calculated as the second spatial derivative of spike amplitude, it is less sensitive to absolute amplitude, and thus the visualization of waveform propagation is more salient. The VIS-FS cluster has a relatively localized current sink centered at the cell body location. In contrast, the VIS-RS1 sCSD profile displayed a traveling wave that propagated unidirectionally upward toward the pia (dorsal direction). Interestingly, the electrode sites below the soma had a current sink earlier than the somatic sink; this is consistent with propagation upward from the spike initiation zone toward the cell body (Kole et al. 2008; Stuart et al. 1997). Finally, the sCSD for the VIS-RS2 waveform was also distinct from the RS1 waveform in that the propagation profile was more symmetric around the cell body and the current sinks did not propagate as far along the probe.

Next, we examined the sCSD for units recorded in the dorsal HP (mostly CA1 region), because backpropagation has also been observed in neurons of this region (Callaway and Ross 1995; Golding et al. 2001; Jung et al. 1997; Spruston et al. 1995). The hippocampus contains both FS and RS units (Hu et al. 2014), so we first used *k*-means clustering to divide units into HP-FS and HP-RS types and then computed the sCSD separately for the two waveform types (Fig. 6B). The HP-FS cluster did not show evidence of backpropagation, but the HP-RS waveform type displayed a clear sink traveling downward along the probe (ventrally). Thus the direction of waveform propagation in HP-RS units was the opposite direction compared with that in VIS-RS1 units. Given the opposite anatomical orientation of dorsal CA1 pyramidal neurons (apical dendrites pointing ventrally) vs. visual cortical pyramidal neurons (apical dendrites pointing dorsally toward pia) (Fig. 1D), this observation provides further evidence that these propagation events correspond to BAPs along apical dendrites. To visualize the propagation direction for each individual unit, we plotted the inverse velocity below vs. above the soma (Fig. 6C). Most VIS-RS1 units have positive velocities both above and below the soma ($P << 0.001$ compared with null distribution), indicating unidirectional propagation toward the pia. These points fall into the top right quadrant of the scatter plot in Fig. 6C. In contrast, many HP-RS units fall into the bottom

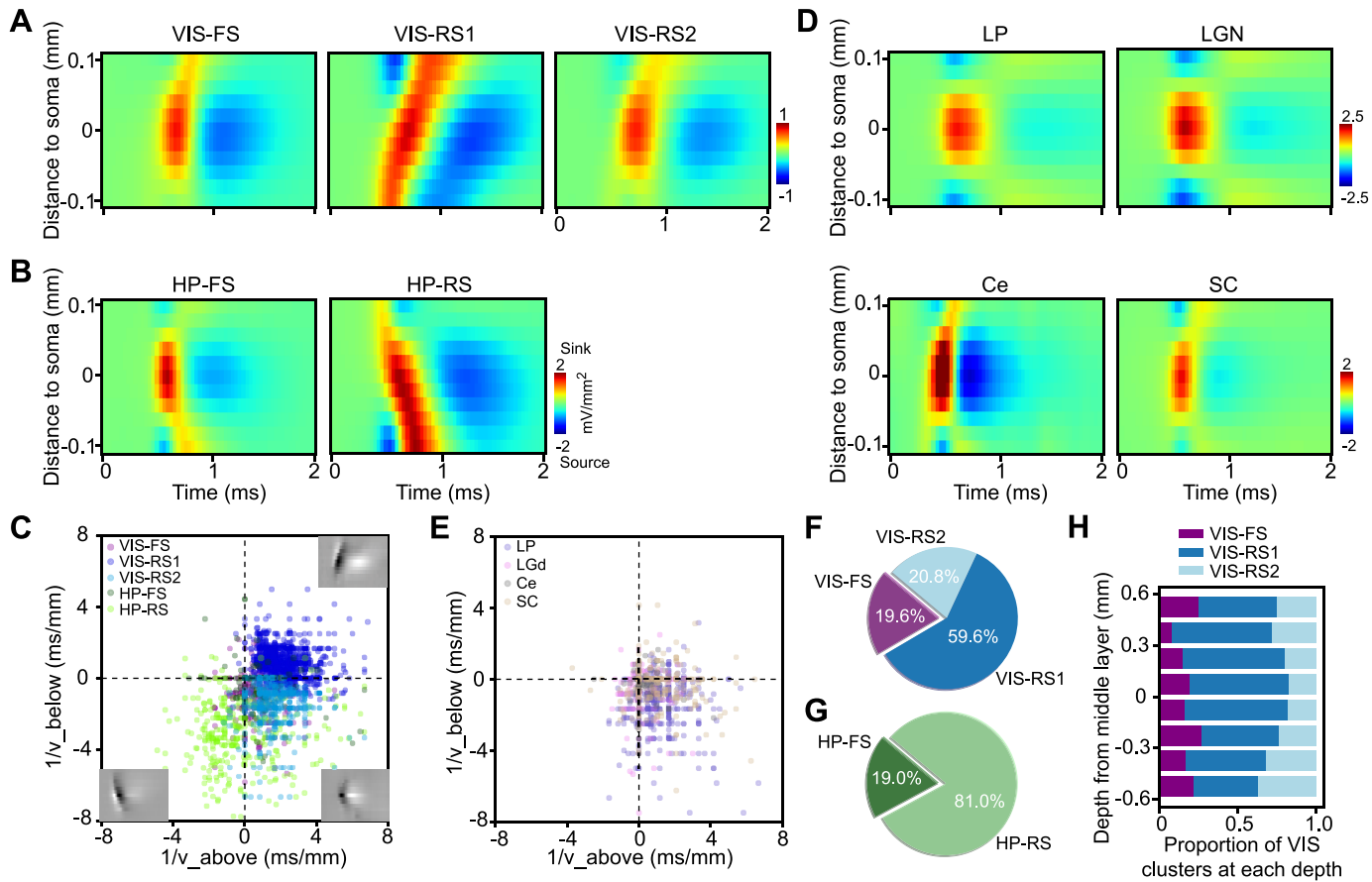


Fig. 6. Action potential backpropagation observed in subclasses of cortical and hippocampal units. *A*: spike-triggered current source density (sCSD) analysis based on the average multichannel waveforms from different clusters in visual cortex (VIS). Propagation toward pia is observed in the regular-spiking neuron type 1 (RS1) cluster (VIS-RS1). *B*: sCSD for fast-spiking (FS) and regular-spiking (RS) clusters in hippocampus (HP). Note opposite direction of spike propagation in HP-RS compared with VIS-RS1 units. *C*: scatter plot of inverse propagation velocity (feature extracted from multichannel waveforms) above ($1/v_{\text{above}}$) and below ($1/v_{\text{below}}$) soma for individual units in visual cortex and hippocampus (same data as shown in Fig. 3*E*). *Top right* quadrant represents units with unidirectional dorsal propagation and is dominated by VIS-RS1 units. *Bottom left* quadrant represents unidirectional propagation ventrally and is dominated by HP-RS units. *Bottom right* quadrant represents bidirectional propagation from soma, which is dominated by FS and VIS-RS2 units. The multichannel waveforms (*insets*) are from example units in 3 quadrants for intuitive illustration. Values closer to 0 indicate faster propagation speed. *D*: sCSD analysis on the average multichannel waveforms from lateral posterior nucleus (LP), lateral geniculate nucleus (LGN), cerebellum (Ce), and superior colliculus (SC). *E*: scatter plot of inverse propagation velocity for LP, LGN, Ce, and SC. Most of the units are in the *bottom right* quadrant, indicating the propagation is bidirectional from soma. *F*: fraction of different subclasses in VIS ($n = 1,609$ units). *G*: fraction of different subclasses in HP ($n = 369$ units). *H*: distribution of waveform clusters in visual cortex as a function of cortical depth relative to layer 4. Middle of layer 4 is denoted as 0 and is estimated using stimulus-evoked CSD (see METHODS and Supplemental Fig. S8).

left quadrant, indicating negative velocities and unidirectional propagation in the opposite direction.

Importantly, because BAPs are only observed in certain cell types with proper channel composition and morphology, they are known to be absent in some cell types, including cerebellar Purkinje cells (Llinás and Sugimori 1980; Stuart and Häusser 1994). Thus we examined the sCSD (Fig. 6*D*) and velocity profile (Fig. 6*E*; Supplemental Fig. S7) for subcortical waveforms recorded from the thalamus (LP, LGN), Ce, and SC. On average, these regions did not show orientated spike propagation along the probe, with most units occupying the *bottom right* quadrant in Fig. 6*E*. However, previous findings showed evidence of BAPs in some subtypes of neurons in SC (Gale and Murphy 2016), which accounts for the observation of some SC units shifted toward the *top right* quadrant of the propagation profile plot in Fig. 6*E* (see also Supplemental Fig. S7).

Both the VIS-RS1 and HP-RS clusters, which show a high incidence of BAPs, represent a significant fraction of recorded units in visual cortex (56.8%; Fig. 6*F*) and hippocampus

(81.0%; Fig. 6*G*). The median velocity of propagation along apical dendrites for VIS-RS1 units is 0.45 ± 0.01 mm/ms, and the median velocity of propagation along apical dendrites for HP-RS units is 0.30 ± 0.06 mm/ms. Because the cortex has a layered structure and most previously measured extracellular BAPs events were identified in layer 5 pyramidal neurons in cortex, we evaluated the VIS-RS1 distribution as a function of cortical depth. Interestingly, VIS-RS1 units were observed across the depth of cortex, indicating that neurons with BAPs exist in all cortical layers *in vivo* in the mouse cortex (Fig. 6*H*; also see Supplemental Fig. S10). The high spatial resolution of Neuropixels probes (20- μm vertical spacing, compared with 50- to 100- μm spacing on other linear probes used in previous studies of BAPs; Bereshpolova et al. 2007; Buzsáki and Kandel 1998) likely provides the ability to detect events propagating over a shorter distance along the dendrite, and this could be the reason we observe BAP-like events in many RS neurons located in different layers of visual cortex rather than only in layer 5 large pyramidal neurons.

DISCUSSION

We sought to determine whether detailed analysis of multi-channel spike waveforms captured on high-density electrode arrays could assist in classification of cell types both within and across different regions of the mouse brain. We measured extracellular action potentials from single units with Neuropixels probes, whose dense recording site arrangement allows detection of extracellular waveforms on multiple probe sites. We found that both 1-channel features, such as waveform duration, and multichannel features, such as propagation profile, were useful for classifying neurons. However, supervised classification showed significant improvement in performance when operating on the multichannel compared with the single-channel waveform, indicating that dense spatial sampling of electrical fields helps to detect cell type-specific morphoelectrical features. Unsupervised clustering of waveforms in the visual cortex revealed FS and RS units but also suggests further division of RS units based on distinct waveform propagation profiles. The propagation profiles of many cortical and hippocampal RS units are strongly indicative of BAPs and demonstrate the potential of the Neuropixels probe for reliable detection of events like BAPs. Finally, we used optotagging to investigate the relationship between our waveform clusters in visual cortex and genetically labeled PV+ inhibitory interneurons. Together, these findings demonstrate the utility of dense extracellular waveforms measured with Neuropixels probes for assisting cell type-specific interrogation of functional circuitry in awake, behaving animals.

Comparison with Previous Studies

Consistent with previous studies (Barthó et al. 2004; Connors and Kriegstein 1986; McCormick et al. 1985; Niell and Stryker 2008; Swadlow 2003), our work confirmed the separation of FS and RS cells and indicated that PV+ neurons are all FS units (Hu et al. 2014). In addition, there are three main aspects that make our study distinct from previous ones. First, the dense sampling of the electrical field by Neuropixels probes allowed us to obtain a rich spatiotemporal profile of the extracellular waveform for each sorted unit. We have shown that this additional information across space, including spread and propagation velocity, provides enhanced classification power and also reveals interesting physiological processes, such as BAPs, which are important for understanding neural computation. BAPs have been studied in a variety of neuron types, including pyramidal cells located in different cortical layers (Stuart et al. 1997; Waters et al. 2005). However, with the use of extracellular recordings in awake, behaving animals, BAPs have been primarily observed in layer 5 pyramidal neurons (Bereshpolova et al. 2007; Buzsáki and Kandel 1998). Our results are the first to demonstrate the potential to record BAPs across layers in behaving animals using extracellular recordings. Second, we compared extracellular waveforms from six brain regions in this study. Because different brain regions may consist of different cell types that express distinct genes and ion channels, we made it an explicit part of our study to compare the diversity of extracellular waveforms from cortical and subcortical brain regions, whereas in the past, most waveform clustering studies have considered spike waveforms only within the local circuit. Third, we applied a diverse set of classification algorithms to analyze cells on the basis of extra-

cellular action potential. Because we localized each unit to an anatomical region in the brain, we could train supervised random forest classifiers to identify features that are important for region-specific cell-type classification. In addition, unsupervised clustering algorithms revealed three waveform types in the visual cortex (FS, RS1, and RS2), suggesting the potential to further divide cortical RS neurons on the basis of extracellular spatiotemporal waveform profiles. However, given the diversity of cell types classified with gene expression (Zeng and Sanes 2017), it is likely both the RS1 and RS2 clusters contain a mixture of neuronal types. Future studies should examine the sensory and behavioral response properties, functional interactions, and genetic profiles of these waveform clusters to identify potential correspondences between these modalities. Optotagging genetically identified neuron types will be particularly helpful to draw these links.

Spike Waveform and Cell Types Across Regions

Our study supports the hypothesis that extracellular waveforms can reflect cell type-specific differences in morphoelectrical properties across brain areas. Multichannel waveforms were distinct across brain regions, likely reflecting the diversity in morphoelectrical properties across areas (Ascoli et al. 2007; Bean 2007; Stuart et al. 1997; Zeng and Sanes 2017). Thalamic excitatory neurons typically show a multipolar soma with numerous and highly branched dendrites in a radial or bipolar distribution (Clascá et al. 2012; Jones 2012). Our results showed symmetric, restricted multichannel waveforms in LGN and LP neurons, consistent with thalamic relay neuron morphology. Additionally, thalamic relay neurons do not show reliable, long-range dendritic backpropagation (Connelly et al. 2017), which is consistent with our results. Interestingly, we could distinctly classify LGN neurons compared with relay neurons in the adjacent higher order thalamic nucleus, LP. A population of LP relay neurons has been identified with relatively long action potential half-width and afterhyperpolarization potentials (Li et al. 2003); this might account for classification accuracy in these regions of the thalamus and is consistent with the longer spike duration and smaller recovery slope we measured in LP neurons. Our recordings from cerebellar cells also support the view that multichannel waveforms reflect morphoelectrical properties. Purkinje cells in the cerebellum have large cell bodies, which can explain the large amplitude and broad spatial spread of the multichannel waveform. However, because the density of dendritic voltage-gated sodium channels of these cells decreases rapidly with distance from the soma, action potential amplitude drops very quickly in the dendrite and fails to invade the dendritic tree (Llinás and Sugimori 1980; Stuart and Häusser 1994; Vetter et al. 2001). Thus Purkinje cells are known to lack, or have highly attenuated, BAPs (Häusser et al. 2000; Stuart et al. 1997), which is consistent with the lack of obvious BAPs in our extracellular recordings of cerebellar cells. In contrast, many RS units in the cortex and hippocampus showed highly directional dendritic backpropagation, suggesting this might be a useful signature for the identification of pyramidal neurons in the cortex and hippocampus.

Exploiting these morphoelectrical differences across areas, we demonstrated the ability to classify neurons across brain regions with extracellular waveforms, which has several im-

plications. First, it is a proof of concept that multichannel waveform analysis can distinguish neurons with distinct morphoelectrical properties. Second, this application could be particularly useful for *in vivo* recordings of dense structures with small nuclei or subdivisions (e.g., other nuclei in thalamus or other subcortical areas) for which purely anatomical registration of units can be especially challenging. Third, the ability to classify cells across brains regions should generalize to other high-density recording probes that also provide spatially dense sampling of spike waveforms. In the future, recordings with even higher density probes (especially with 2- or 3-dimensional coverage) will enhance the ability to identify cell types purely on the basis of extracellular signals. Dense three-dimensional sampling could generate “electrical images” that capture fine-scale nuances in morphoelectrical properties and allow cross-experiment registration of neurons independently of the geometric alignment of the probe and recorded neurons.

Backpropagating Action Potentials

BAPs are active events that propagate from the spike initiation zone, invade the soma, and then travel along dendrites via depolarization of voltage-gated sodium channels or calcium channels (Häusser et al. 2000; Stuart et al. 1997; Waters et al. 2005). BAPs have been studied *in vitro* and *in vivo* using both dendritic electrical recording and imaging methodologies (Callaway and Ross 1995; Jung et al. 1997; Kaiser et al. 2001; Kamondi et al. 1998; Martina et al. 2000; Shai 2016; Spruston et al. 1995; Stuart et al. 1997; Svoboda et al. 1997; Waters et al. 2005). Interestingly, different neuronal types can show differences in BAPs, which are caused by a combination of both channel density and dendritic morphology (Häusser et al. 2000; Stuart et al. 1997; Vetter et al. 2001). In pyramidal neurons, BAPs can serve important computational roles, including providing a mechanism for synaptic plasticity (Magee and Johnston 1997; Markram et al. 1997) and supporting dendritic integration of bottom-up and top-down signals (Larkum et al. 1999; Siegel et al. 2000). Moreover, BAPs might be subject to dynamic modulation by behavioral experience (Quirk et al. 2001; but see Bereshpolova et al. 2007). Therefore, the ability to routinely measure BAPs in behaving animals and associate them with functional response properties will be of great physiological importance for understanding the computational roles of spike backpropagation (Häusser et al. 2000; Linden 1999; Sjöström and Häusser 2006).

Two previous studies have used linear multichannel extracellular electrode arrays to investigate BAPs in the sensory cortex of awake rat (Buzsáki and Kandel 1998) and rabbit (Bereshpolova et al. 2007). In both cases, the units displaying BAPs were layer 5 RS units; importantly, FS interneurons did not show these traveling waves. In our study, the enhanced spatial sampling from the Neuropixels probe revealed that many units in the hippocampus and cortex had dendritic propagation events across different layers. We also compared the measured BAPs parameters with previous studies. BAPs measured in the rat traveled up to 400 μm in distance (Buzsáki and Kandel 1998) and up to 800 μm in rabbit (Bereshpolova et al. 2007), whereas the maximum spread of BAPs we measured is 380 μm (with a mean of 160 μm), which is similar to that in rat but shorter than in rabbit. Previous studies also showed faster propagation speed of BAPs [0.67 m/s from Buzsáki and

Kandel (1998) and 0.78 m/s from Bereshpolova et al. (2007)] compared with ours (0.54 m/s on average). There are several factors that could account for these differences. First, the previous studies took great care to perfectly align the linear probe parallel with the apical dendrites of layer 5 pyramidal neurons. In our study, we did not explicitly require such rigorous alignment, and this could lead to an underestimation of the distance traveled and the speed of propagation, because the apical dendrite might diverge away from the probe. Nonetheless, our primary goal was to identify features of spikes that can differentiate cell types, and thus capturing the first 100–200 μm of BAP travel was sufficient for this purpose. Second, we sought to record many neurons simultaneously and across layers instead of tailoring the recording to one or a few perfectly aligned large and extended layer 5 neurons. Thus the shorter apical dendrites of layer 4 and layer 2/3 neurons may contribute to the smaller averaged BAPs spread we measured. Third, the mouse cortex is not as thick as that of larger mammals, and in addition, the morphological and electrical properties of pyramidal apical dendrites may differ across species.

Future Studies

Although our present focus was on spike waveform features, future studies of cell classification could include additional information related to spiking firing rates, bursting, and adaptation (Nowak et al. 2003), spike-train autocorrelation (Ebbesen et al. 2016; English et al. 2017), and cross-correlation analysis to define excitatory and inhibitory cells by inferring monosynaptic functional interactions (Barthó et al. 2004; Sirota et al. 2008). Combining multichannel waveforms and spike train features should provide even greater power to reveal distinct cell type-specific properties useful for classification from purely electrophysiological recordings *in vivo*. In addition, biophysical modeling can provide important information about how cell type-specific morphoelectrical features are reflected in the extracellular spike waveform and how this depends on factors such as electrode sampling density and probe geometry (Buccino et al. 2018). An important ultimate use of the waveform analysis methods we describe is to study the response properties of different cell classes and their functional roles in complex neural networks. Neuropixels and other high-density probes (Neto et al. 2016; Rios et al. 2016; Scholvin et al. 2016; Shobe et al. 2015) are now being used to generate large-scale data sets in the brain of awake mice performing a variety of sensory, behavioral, and cognitive tasks. Waveform analysis should aid in cell-type identification *in vivo* and may also reveal the physiological spike properties such as BAPs that could provide additional insight into the functional logic of neural circuit operations.

ACKNOWLEDGMENTS

We thank Ali Williford and Jennifer Luviano for help with surgical procedures, Gregg Heller for help running experiments, Shiella Caldejon for performing intrinsic signal imaging, Timothy Cox for help with tissue clearing and OPT imaging, Will Allen for advice on brain clearing techniques, and Marius Pachitariu for help with the spike sorting algorithm. We thank the Allen Institute for Brain Science founder, Paul G. Allen, for his vision, encouragement, and support.

GRANTS

The work was supported by the Allen Institute for Brain Science.

DISCLOSURES

No conflicts of interest, financial or otherwise, are declared by the authors.

AUTHOR CONTRIBUTIONS

X.J. and S.R.O conceived and designed research; J.H.S., C.B., S.D.G., and D.J.D. performed experiments; X.J. analyzed data; X.J., C.K., and S.R.O. interpreted results of experiments; X.J., J.H.S., C.B., S.D.G., and D.J.D. prepared figures; X.J. drafted manuscript; X.J., J.H.S., C.B., S.D.G., D.J.D., C.K., and S.R.O. edited and revised manuscript; X.J. and S.R.O. approved final version of manuscript.

REFERENCES

- Anastassiou CA, Perin R, Buzsáki G, Markram H, Koch C. Cell type- and activity-dependent extracellular correlates of intracellular spiking. *J Neurophysiol* 114: 608–623, 2015. doi:[10.1152/jn.00628.2014](https://doi.org/10.1152/jn.00628.2014).
- Andermann ML, Ritt J, Neimark MA, Moore CI. Neural correlates of vibrissa resonance; band-pass and somatotopic representation of high-frequency stimuli. *Neuron* 42: 451–463, 2004. doi:[10.1016/S0896-6273\(04\)00198-9](https://doi.org/10.1016/S0896-6273(04)00198-9).
- Ascoli GA, Donohue DE, Halavi M. NeuroMorpho.org: a central resource for neuronal morphologies. *J Neurosci* 27: 9247–9251, 2007. doi:[10.1523/JNEUROSCI.2055-07.2007](https://doi.org/10.1523/JNEUROSCI.2055-07.2007).
- Baden T, Berens P, Franke K, Román Rosón M, Bethge M, Euler T. The functional diversity of retinal ganglion cells in the mouse. *Nature* 529: 345–350, 2016. doi:[10.1038/nature16468](https://doi.org/10.1038/nature16468).
- Báthó P, Hirase H, Monconduit L, Zugaro M, Harris KD, Buzsáki G. Characterization of neocortical principal cells and interneurons by network interactions and extracellular features. *J Neurophysiol* 92: 600–608, 2004. doi:[10.1152/jn.01170.2003](https://doi.org/10.1152/jn.01170.2003).
- Bean BP. The action potential in mammalian central neurons. *Nat Rev Neurosci* 8: 451–465, 2007. doi:[10.1038/nrn2148](https://doi.org/10.1038/nrn2148).
- Bereshepolova Y, Amitai Y, Gusev AG, Stoelzel CR, Swadlow HA. Dendritic backpropagation and the state of the awake neocortex. *J Neurosci* 27: 9392–9399, 2007. doi:[10.1523/JNEUROSCI.2218-07.2007](https://doi.org/10.1523/JNEUROSCI.2218-07.2007).
- Blanche TJ, Spacek MA, Hetke JF, Swindale NV. Polytrodes: high-density silicon electrode arrays for large-scale multiunit recording. *J Neurophysiol* 93: 2987–3000, 2005. doi:[10.1152/jn.01023.2004](https://doi.org/10.1152/jn.01023.2004).
- Bortone DS, Olsen SR, Scanziani M. Translaminar inhibitory cells recruited by layer 6 corticothalamic neurons suppress visual cortex. *Neuron* 82: 474–485, 2014. doi:[10.1016/j.neuron.2014.02.021](https://doi.org/10.1016/j.neuron.2014.02.021).
- Breiman L, Friedman J, Olshen RA, Stone CJ. *Classification and Regression Trees*. Belmont, CA: Wadsworth, 1984.
- Bruno RM, Simons DJ. Feedforward mechanisms of excitatory and inhibitory cortical receptive fields. *J Neurosci* 22: 10966–10975, 2002. doi:[10.1523/JNEUROSCI.22-24-10966.2002](https://doi.org/10.1523/JNEUROSCI.22-24-10966.2002).
- Buccino AP, Kordovan M, Ness TV, Merkt B, Häfliger PD, Fyhn M, Cauwenberghs G, Rotter S, Einevoll GT. Combining biophysical modeling and deep learning for multielectrode array neuron localization and classification. *J Neurophysiol* 120: 1212–1232, 2018. doi:[10.1152/jn.00210.2018](https://doi.org/10.1152/jn.00210.2018).
- Buzsáki G, Anastassiou CA, Koch C. The origin of extracellular fields and currents—EEG, ECoG, LFP and spikes. *Nat Rev Neurosci* 13: 407–420, 2012. doi:[10.1038/nrn3241](https://doi.org/10.1038/nrn3241).
- Buzsáki G, Kandel A. Somadendritic backpropagation of action potentials in cortical pyramidal cells of the awake rat. *J Neurophysiol* 79: 1587–1591, 1998. doi:[10.1152/jn.1998.79.3.1587](https://doi.org/10.1152/jn.1998.79.3.1587).
- Callaway JC, Ross WN. Frequency-dependent propagation of sodium action potentials in dendrites of hippocampal CA1 pyramidal neurons. *J Neurophysiol* 74: 1395–1403, 1995. doi:[10.1152/jn.1995.74.4.1395](https://doi.org/10.1152/jn.1995.74.4.1395).
- Chung JE, Joo HR, Fan JL, Liu DF, Barnett AH, Chen S, Geaghan-Breiner C, Karlsson MP, Karlsson M, Lee KY, Liang H, Magland JF, Tooker AC, Greengard LF, Tolosa VM, Frank LM. High-density, long-lasting, and multi-region electrophysiological recordings using polymer electrode arrays (Preprint). *bioRxiv* 242693, 2018. doi:[10.1101/242693](https://doi.org/10.1101/242693).
- Clascá F, Rubio-Garrido P, Jabaudon D. Unveiling the diversity of thalamocortical neuron subtypes. *Eur J Neurosci* 35: 1524–1532, 2012. doi:[10.1111/j.1460-9568.2012.08033.x](https://doi.org/10.1111/j.1460-9568.2012.08033.x).
- Cohen JY, Haesler S, Vong L, Lowell BB, Uchida N. Neuron-type-specific signals for reward and punishment in the ventral tegmental area. *Nature* 482: 85–88, 2012. doi:[10.1038/nature10754](https://doi.org/10.1038/nature10754).
- Connelly WM, Crunelli V, Errington AC. Variable action potential back-propagation during tonic firing and low-threshold spike bursts in thalamocortical but not thalamic reticular nucleus neurons. *J Neurosci* 37: 5319–5333, 2017. doi:[10.1523/JNEUROSCI.0015-17.2017](https://doi.org/10.1523/JNEUROSCI.0015-17.2017).
- Connors BW, Kriegstein AR. Cellular physiology of the turtle visual cortex: distinctive properties of pyramidal and stellate neurons. *J Neurosci* 6: 164–177, 1986. doi:[10.1523/JNEUROSCI.06-01-00164.1986](https://doi.org/10.1523/JNEUROSCI.06-01-00164.1986).
- Delgado Ruiz I, Schultz SR. Localising and classifying neurons from high density MEA recordings. *J Neurosci Methods* 233: 115–128, 2014. doi:[10.1016/j.jneumeth.2014.05.037](https://doi.org/10.1016/j.jneumeth.2014.05.037).
- Ebbesen CL, Reifenstein ET, Tang Q, Burgalossi A, Ray S, Schreiber S, Kemper R, Brecht M. Cell type-specific differences in spike timing and spike shape in the rat parasubiculum and superficial medial entorhinal cortex. *Cell Rep* 16: 1005–1015, 2016. doi:[10.1016/j.celrep.2016.06.057](https://doi.org/10.1016/j.celrep.2016.06.057).
- English DF, McKenzie S, Evans T, Kim K, Yoon E, Buzsáki G. Pyramidal Cell-Interneuron Circuit Architecture and Dynamics in Hippocampal Networks. *Neuron* 96: 505–520.e7, 2017. doi:[10.1016/j.neuron.2017.09.033](https://doi.org/10.1016/j.neuron.2017.09.033).
- Gale SD, Murphy GJ. Active dendritic properties and local inhibitory input enable selectivity for object motion in mouse superior colliculus neurons. *J Neurosci* 36: 9111–9123, 2016. doi:[10.1523/JNEUROSCI.0645-16.2016](https://doi.org/10.1523/JNEUROSCI.0645-16.2016).
- Gold C, Henze DA, Koch C, Buzsáki G. On the origin of the extracellular action potential waveform: A modeling study. *J Neurophysiol* 95: 3113–3128, 2006. doi:[10.1152/jn.00979.2005](https://doi.org/10.1152/jn.00979.2005).
- Golding NL, Kath WL, Spruston N. Dichotomy of action-potential back-propagation in CA1 pyramidal neuron dendrites. *J Neurophysiol* 86: 2998–3010, 2001. doi:[10.1152/jn.2001.86.6.2998](https://doi.org/10.1152/jn.2001.86.6.2998).
- Gouwens NW, Berg J, Feng D, Sorensen SA, Zeng H, Hawrylycz MJ, Koch C, Arkhipov A. Systematic generation of biophysically detailed models for diverse cortical neuron types. *Nat Commun* 9: 710, 2018. doi:[10.1038/s41467-017-02718-3](https://doi.org/10.1038/s41467-017-02718-3).
- Hangya B, Ranade SP, Lorenc M, Képés A. Central cholinergic neurons are rapidly recruited by reinforcement feedback. *Cell* 162: 1155–1168, 2015. doi:[10.1016/j.cell.2015.07.057](https://doi.org/10.1016/j.cell.2015.07.057).
- Harris KD, Shepherd GMG. The neocortical circuit: themes and variations. *Nat Neurosci* 18: 170–181, 2015. doi:[10.1038/nn.3917](https://doi.org/10.1038/nn.3917).
- Hasenstaub A, Shu Y, Haider B, Kraushaar U, Duque A, McCormick DA. Inhibitory postsynaptic potentials carry synchronized frequency information in active cortical networks. *Neuron* 47: 423–435, 2005. doi:[10.1016/j.neuron.2005.06.016](https://doi.org/10.1016/j.neuron.2005.06.016).
- Häusser M, Spruston N, Stuart GJ. Diversity and dynamics of dendritic signaling. *Science* 290: 739–744, 2000. doi:[10.1126/science.290.5492.739](https://doi.org/10.1126/science.290.5492.739).
- Henze DA, Borhegyi Z, Csicsvari J, Mamiya A, Harris KD, Buzsáki G. Intracellular features predicted by extracellular recordings in the hippocampus *in vivo*. *J Neurophysiol* 84: 390–400, 2000. doi:[10.1152/jn.2000.84.1.390](https://doi.org/10.1152/jn.2000.84.1.390).
- Heo C, Park H, Kim YT, Baeg E, Kim YH, Kim S-G, Suh M. A soft, transparent, freely accessible cranial window for chronic imaging and electrophysiology. *Sci Rep* 6: 27818, 2016. doi:[10.1038/srep27818](https://doi.org/10.1038/srep27818).
- Hu H, Gan J, Jonas P. Interneurons. Fast-spiking, parvalbumin⁺ GABAergic interneurons: from cellular design to microcircuit function. *Science* 345: 1255263, 2014. doi:[10.1126/science.1255263](https://doi.org/10.1126/science.1255263).
- Isaacson JS, Scanziani M. How inhibition shapes cortical activity. *Neuron* 72: 231–243, 2011. doi:[10.1016/j.neuron.2011.09.027](https://doi.org/10.1016/j.neuron.2011.09.027).
- Jiang X, Shen S, Cadwell CR, Berens P, Sinz F, Ecker AS, Patel S, Tolias AS. Principles of connectivity among morphologically defined cell types in adult neocortex. *Science* 350: aac9462, 2015. doi:[10.1126/science.aac9462](https://doi.org/10.1126/science.aac9462).
- Jones EG. *The Thalamus*. New York: Springer Science & Business Media, 2012.
- Juavinett AL, Nauhaus I, Garrett ME, Zhuang J, Callaway EM. Automated identification of mouse visual areas with intrinsic signal imaging. *Nat Protoc* 12: 32–43, 2017. doi:[10.1038/nprot.2016.158](https://doi.org/10.1038/nprot.2016.158).
- Jun JJ, Steinmetz NA, Siegle JH, Denman DJ, Bauza M, Barabasi B, Lee AK, Anastassiou CA, Andrei A, Aydin Ç, Barbic M, Blanche TJ, Bonin V, Couto J, Dutta B, Gratton SL, Gutnisky DA, Häusser M, Karsh B, Ledochowitsch P, Lopez CM, Mitelut C, Musa S, Okun M, Pachitariu M, Putzeys J, Rich PD, Rossant C, Sun WL, Svoboda K, Carandini M, Harris KD, Koch C, O’Keefe J, Harris TD. Fully integrated silicon probes for high-density recording of neural activity. *Nature* 551: 232–236, 2017. doi:[10.1038/nature24636](https://doi.org/10.1038/nature24636).
- Jung HY, Mickus T, Spruston N. Prolonged sodium channel inactivation contributes to dendritic action potential attenuation in hippocampal pyramidal

- dal neurons. *J Neurosci* 17: 6639–6646, 1997. doi:[10.1523/JNEUROSCI.17-17-06639.1997](https://doi.org/10.1523/JNEUROSCI.17-17-06639.1997).
- Kaiser KM, Zilberter Y, Sakmann B.** Back-propagating action potentials mediate calcium signalling in dendrites of bifurcating interneurons in layer 2/3 of rat somatosensory cortex. *J Physiol* 535: 17–31, 2001. doi:[10.1111/j.1469-7793.2001.t01-1-00017.x](https://doi.org/10.1111/j.1469-7793.2001.t01-1-00017.x).
- Kamondi A, Acsády L, Buzsáki G.** Dendritic spikes are enhanced by cooperative network activity in the intact hippocampus. *J Neurosci* 18: 3919–3928, 1998. doi:[10.1523/JNEUROSCI.18-10-03919.1998](https://doi.org/10.1523/JNEUROSCI.18-10-03919.1998).
- Kawaguchi Y.** Groupings of nonpyramidal and pyramidal cells with specific physiological and morphological characteristics in rat frontal cortex. *J Neurophysiol* 69: 416–431, 1993. doi:[10.1152/jn.1993.69.2.416](https://doi.org/10.1152/jn.1993.69.2.416).
- Kepes A, Fishell G.** Interneuron cell types are fit to function. *Nature* 505: 318–326, 2014. doi:[10.1038/nature12983](https://doi.org/10.1038/nature12983).
- Kim Y, Yang GR, Pradhan K, Venkataraju KU, Bota M, García Del Molino LC, Fitzgerald G, Ram K, He M, Levine JM, Mitra P, Huang ZJ, Wang XJ, Osten P.** Brain-wide maps reveal stereotyped cell-type-based cortical architecture and subcortical sexual dimorphism. *Cell* 171: 456–469.e22, 2017. doi:[10.1016/j.cell.2017.09.020](https://doi.org/10.1016/j.cell.2017.09.020).
- Kole MH, Illeschner SU, Kampa BM, Williams SR, Ruben PC, Stuart GJ.** Action potential generation requires a high sodium channel density in the axon initial segment. *Nat Neurosci* 11: 178–186, 2008. doi:[10.1038/nn2040](https://doi.org/10.1038/nn2040).
- Kvitsiani D, Ranade S, Hangya B, Taniguchi H, Huang JZ, Kepes A.** Distinct behavioural and network correlates of two interneuron types in prefrontal cortex. *Nature* 498: 363–366, 2013. doi:[10.1038/nature12176](https://doi.org/10.1038/nature12176).
- Larkum ME, Zhu JJ, Sakmann B.** A new cellular mechanism for coupling inputs arriving at different cortical layers. *Nature* 398: 338–341, 1999. doi:[10.1038/18686](https://doi.org/10.1038/18686).
- Li J, Bickford ME, Guido T.** Distinct firing properties of higher order thalamic relay neurons. *J Neurophysiol* 90: 291–299, 2003. doi:[10.1152/jn.01163.2002](https://doi.org/10.1152/jn.01163.2002).
- Li N, Chen T-W, Guo ZV, Gerfen CR, Svoboda K.** A motor cortex circuit for motor planning and movement. *Nature* 519: 51–56, 2015. doi:[10.1038/nature14178](https://doi.org/10.1038/nature14178).
- Lima SQ, Hromádka T, Znamenskiy P, Zador AM.** PINP: a new method of tagging neuronal populations for identification during *in vivo* electrophysiological recording. *PLoS One* 4: e6099, 2009. doi:[10.1371/journal.pone.0006099](https://doi.org/10.1371/journal.pone.0006099).
- Linden DJ.** The return of the spike: postsynaptic action potentials and the induction of LTP and LTD. *Neuron* 22: 661–666, 1999. doi:[10.1016/S0896-6273\(00\)80726-6](https://doi.org/10.1016/S0896-6273(00)80726-6).
- Lipski J.** Antidromic activation of neurones as an analytic tool in the study of the central nervous system. *J Neurosci Methods* 4: 1–32, 1981. doi:[10.1016/0165-0270\(81\)90015-7](https://doi.org/10.1016/0165-0270(81)90015-7).
- Llinás R, Sugimori M.** Electrophysiological properties of *in vitro* Purkinje cell dendrites in mammalian cerebellar slices. *J Physiol* 305: 197–213, 1980. doi:[10.1113/jphysiol.1980.sp013358](https://doi.org/10.1113/jphysiol.1980.sp013358).
- Luo L, Callaway EM, Svoboda K.** Genetic dissection of neural circuits. *Neuron* 57: 634–660, 2008. doi:[10.1016/j.neuron.2008.01.002](https://doi.org/10.1016/j.neuron.2008.01.002).
- Magee JC, Johnston D.** A synaptically controlled, associative signal for Hebbian plasticity in hippocampal neurons. *Science* 275: 209–213, 1997. doi:[10.1126/science.275.5297.209](https://doi.org/10.1126/science.275.5297.209).
- Markram H, Lübke J, Frotscher M, Sakmann B.** Regulation of synaptic efficacy by coincidence of postsynaptic APs and EPSPs. *Science* 275: 213–215, 1997. doi:[10.1126/science.275.5297.213](https://doi.org/10.1126/science.275.5297.213).
- Markram H, Toledo-Rodriguez M, Wang Y, Gupta A, Silberberg G, Wu C.** Interneurons of the neocortical inhibitory system. *Nat Rev Neurosci* 5: 793–807, 2004. doi:[10.1038/nrn1519](https://doi.org/10.1038/nrn1519).
- Martina M, Vida I, Jonas P.** Distal initiation and active propagation of action potentials in interneuron dendrites. *Science* 287: 295–300, 2000. doi:[10.1126/science.287.5451.295](https://doi.org/10.1126/science.287.5451.295).
- McCormick DA, Connors BW, Lighthall JW, Prince DA.** Comparative electrophysiology of pyramidal and sparsely spiny stellate neurons of the neocortex. *J Neurophysiol* 54: 782–806, 1985. doi:[10.1152/jn.1985.54.4.782](https://doi.org/10.1152/jn.1985.54.4.782).
- Mitchell JF, Sundberg KA, Reynolds JH.** Differential attention-dependent response modulation across cell classes in macaque visual area V4. *Neuron* 55: 131–141, 2007. doi:[10.1016/j.neuron.2007.06.018](https://doi.org/10.1016/j.neuron.2007.06.018).
- Neto JP, Lopes G, Frazão J, Nogueira J, Lacerda P, Baião P, Aarts A, Andrei A, Musa S, Fortunato E, Barquinha P, Kampff AR.** Validating silicon polytrodes with paired juxtacellular recordings: method and dataset. *J Neurophysiol* 116: 892–903, 2016. doi:[10.1152/jn.00103.2016](https://doi.org/10.1152/jn.00103.2016).
- Nowak LG, Azouz R, Sanchez-Vives MV, Gray CM, McCormick DA.** Electrophysiological classes of cat primary visual cortical neurons *in vivo* as revealed by quantitative analyses. *J Neurophysiol* 89: 1541–1566, 2003. doi:[10.1152/jn.00580.2002](https://doi.org/10.1152/jn.00580.2002).
- Pachitariu M, Steinmetz N, Kadir S, Carandini M, Harris KD.** Kilosort: realtime spike-sorting for extracellular electrophysiology with hundreds of channels. *bioRxiv* 061481, 2016. doi:[10.1101/061481](https://doi.org/10.1101/061481).
- Pedregosa F, Varoquaux G, Gramfort A, Michel V, Thirion B, Grisel O, Blondel M, Prettenhofer P, Weiss R, Dubourg V, Vanderplas J, Passos A, Cournapeau D, Brucher M, Perrot M, Duchesnay É.** Scikit-learn: machine learning in Python. *J Mach Learn Res* 12: 2825–2830, 2011.
- Peyrache A, Dehghani N, Eskandar EN, Madsen JR, Anderson WS, Donoghue JA, Hochberg LR, Halgren E, Cash SS, Destexhe A.** Spatio-temporal dynamics of neocortical excitation and inhibition during human sleep. *Proc Natl Acad Sci USA* 109: 1731–1736, 2012. doi:[10.1073/pnas.1109895109](https://doi.org/10.1073/pnas.1109895109).
- Pham DT, Dimov SS, Nguyen CD.** Selection of K in K -means clustering. *Proc Inst Mech Eng C J Mech Eng Sci* 219: 103–119, 2005. doi:[10.1243/095440605X8298](https://doi.org/10.1243/095440605X8298).
- Quirk MC, Blum KI, Wilson MA.** Experience-dependent changes in extracellular spike amplitude may reflect regulation of dendritic action potential back-propagation in rat hippocampal pyramidal cells. *J Neurosci* 21: 240–248, 2001. doi:[10.1523/JNEUROSCI.21-01-00240.2001](https://doi.org/10.1523/JNEUROSCI.21-01-00240.2001).
- Rios G, Lubenov EV, Chi D, Roukes ML, Siapas AG.** Nanofabricated neural probes for dense 3-D recordings of brain activity. *Nano Lett* 16: 6857–6862, 2016. doi:[10.1021/acs.nanolett.6b02673](https://doi.org/10.1021/acs.nanolett.6b02673).
- Rossant C, Kadir SN, Goodman DF, Schulman J, Hunter ML, Saleem AB, Grosmark A, Belluscio M, Denfield GH, Ecker AS, Tolias AS, Solomon S, Buzsáki G, Carandini M, Harris KD.** Spike sorting for large, dense electrode arrays. *Nat Neurosci* 19: 634–641, 2016. doi:[10.1038/nn.4268](https://doi.org/10.1038/nn.4268).
- Rutherford P, Paul O.** New approaches for CMOS-based devices for large-scale neural recording. *Curr Opin Neurobiol* 32: 31–37, 2015. doi:[10.1016/j.conb.2014.10.007](https://doi.org/10.1016/j.conb.2014.10.007).
- Scholvin J, Kinney JP, Bernstein JG, Moore-Kochlacs C, Kopell N, Fonstad CG, Boyden ES.** Close-packed silicon microelectrodes for scalable spatially oversampled neural recording. *IEEE Trans Biomed Eng* 63: 120–130, 2016. doi:[10.1109/TBME.2015.2406113](https://doi.org/10.1109/TBME.2015.2406113).
- Shai A.** *The Physiology and Computation of Pyramidal Neurons* (Dissertation). Pasadena, CA: California Institute of Technology, 2016.
- Shobe JL, Claar LD, Parhami S, Bakhurin KI, Masmanidis SC.** Brain activity mapping at multiple scales with silicon micropores containing 1,024 electrodes. *J Neurophysiol* 114: 2043–2052, 2015. doi:[10.1152/jn.00464.2015](https://doi.org/10.1152/jn.00464.2015).
- Siegel M, Körding KP, König P.** Integrating top-down and bottom-up sensory processing by somato-dendritic interactions. *J Comput Neurosci* 8: 161–173, 2000. doi:[10.1023/A:1008973215925](https://doi.org/10.1023/A:1008973215925).
- Siegle JH, López AC, Patel YA, Abramov K, Ohayon S, Voigts J.** Open Ephys: an open-source, plugin-based platform for multichannel electrophysiology. *J Neural Eng* 14: 045003, 2017. doi:[10.1088/1741-2552/aa5ee4](https://doi.org/10.1088/1741-2552/aa5ee4).
- Sirota A, Montgomery S, Fujisawa S, Isomura Y, Zugaro M, Buzsáki G.** Entrainment of neocortical neurons and gamma oscillations by the hippocampal theta rhythm. *Neuron* 60: 683–697, 2008. doi:[10.1016/j.neuron.2008.09.014](https://doi.org/10.1016/j.neuron.2008.09.014).
- Sjöström PJ, Häusser M.** A cooperative switch determines the sign of synaptic plasticity in distal dendrites of neocortical pyramidal neurons. *Neuron* 51: 227–238, 2006. doi:[10.1016/j.neuron.2006.06.017](https://doi.org/10.1016/j.neuron.2006.06.017).
- Smith MA, Jia X, Zandvakili A, Kohn A.** Laminar dependence of neuronal correlations in visual cortex. *J Neurophysiol* 109: 940–947, 2013. doi:[10.1152/jn.00846.2012](https://doi.org/10.1152/jn.00846.2012).
- Sommer MA, Wurtz RH.** What the brain stem tells the frontal cortex. I. Oculomotor signals sent from superior colliculus to frontal eye field via mediodorsal thalamus. *J Neurophysiol* 91: 1381–1402, 2004. doi:[10.1152/jn.00738.2003](https://doi.org/10.1152/jn.00738.2003).
- Spruston N.** Pyramidal neurons: dendritic structure and synaptic integration. *Nat Rev Neurosci* 9: 206–221, 2008. doi:[10.1038/nrn2286](https://doi.org/10.1038/nrn2286).
- Spruston N, Schiller Y, Stuart G, Sakmann B.** Activity-dependent action potential invasion and calcium influx into hippocampal CA1 dendrites. *Science* 268: 297–300, 1995. doi:[10.1126/science.7716524](https://doi.org/10.1126/science.7716524).
- Stoezel CR, Bereshpolova Y, Swadlow HA.** Stability of thalamocortical synaptic transmission across awake brain states. *J Neurosci* 29: 6851–6859, 2009. doi:[10.1523/JNEUROSCI.5983-08.2009](https://doi.org/10.1523/JNEUROSCI.5983-08.2009).

- Stuart G, Häusser M.** Initiation and spread of sodium action potentials in cerebellar Purkinje cells. *Neuron* 13: 703–712, 1994. doi:[10.1016/0896-6273\(94\)90037-X](https://doi.org/10.1016/0896-6273(94)90037-X).
- Stuart G, Spruston N, Sakmann B, Häusser M.** Action potential initiation and back propagation in neurons of the mammalian central nervous system. *Trends Neurosci* 20: 125–131, 1997. doi:[10.1016/S0166-2236\(96\)10075-8](https://doi.org/10.1016/S0166-2236(96)10075-8).
- Stuart GJ, Sakmann B.** Active propagation of somatic action potentials into neocortical pyramidal cell dendrites. *Nature* 367: 69–72, 1994. doi:[10.1038/367069a0](https://doi.org/10.1038/367069a0).
- Svoboda K, Denk W, Kleinfeld D, Tank DW.** In vivo dendritic calcium dynamics in neocortical pyramidal neurons. *Nature* 385: 161–165, 1997. doi:[10.1038/385161a0](https://doi.org/10.1038/385161a0).
- Swadlow HA.** Fast-spike interneurons and feedforward inhibition in awake sensory neocortex. *Cereb Cortex* 13: 25–32, 2003. doi:[10.1093/cercor/13.1.25](https://doi.org/10.1093/cercor/13.1.25).
- Tasic B, Menon V, Nguyen TN, Kim TK, Jarsky T, Yao Z, Levi B, Gray LT, Sorensen SA, Dolbeare T, Bertagnolli D, Goldy J, Shapovalova N, Parry S, Lee C, Smith K, Bernard A, Madisen L, Sunkin SM, Hawry-**
- Iycz M, Koch C, Zeng H.** Adult mouse cortical cell taxonomy revealed by single cell transcriptomics. *Nat Neurosci* 19: 335–346, 2016. doi:[10.1038/nn.4216](https://doi.org/10.1038/nn.4216).
- van der Maaten L, Hinton G.** Visualizing data using t-SNE. *J Mach Learn Res* 9: 2579–2605, 2008.
- Vetter P, Roth A, Häusser M.** Propagation of action potentials in dendrites depends on dendritic morphology. *J Neurophysiol* 85: 926–937, 2001. doi:[10.1152/jn.2001.85.2.926](https://doi.org/10.1152/jn.2001.85.2.926).
- Waters J, Schaefer A, Sakmann B.** Backpropagating action potentials in neurones: measurement, mechanisms and potential functions. *Prog Biophys Mol Biol* 87: 145–170, 2005. doi:[10.1016/j.pbiomolbio.2004.06.009](https://doi.org/10.1016/j.pbiomolbio.2004.06.009).
- Weir K, Blanquie O, Kilb W, Luhmann HJ, Sinning A.** Comparison of spike parameters from optically identified GABAergic and glutamatergic neurons in sparse cortical cultures. *Front Cell Neurosci* 8: 460, 2015. doi:[10.3389/fncel.2014.00460](https://doi.org/10.3389/fncel.2014.00460).
- Zeng H, Sanes JR.** Neuronal cell-type classification: challenges, opportunities and the path forward. *Nat Rev Neurosci* 18: 530–546, 2017. doi:[10.1038/nrn.2017.85](https://doi.org/10.1038/nrn.2017.85).

